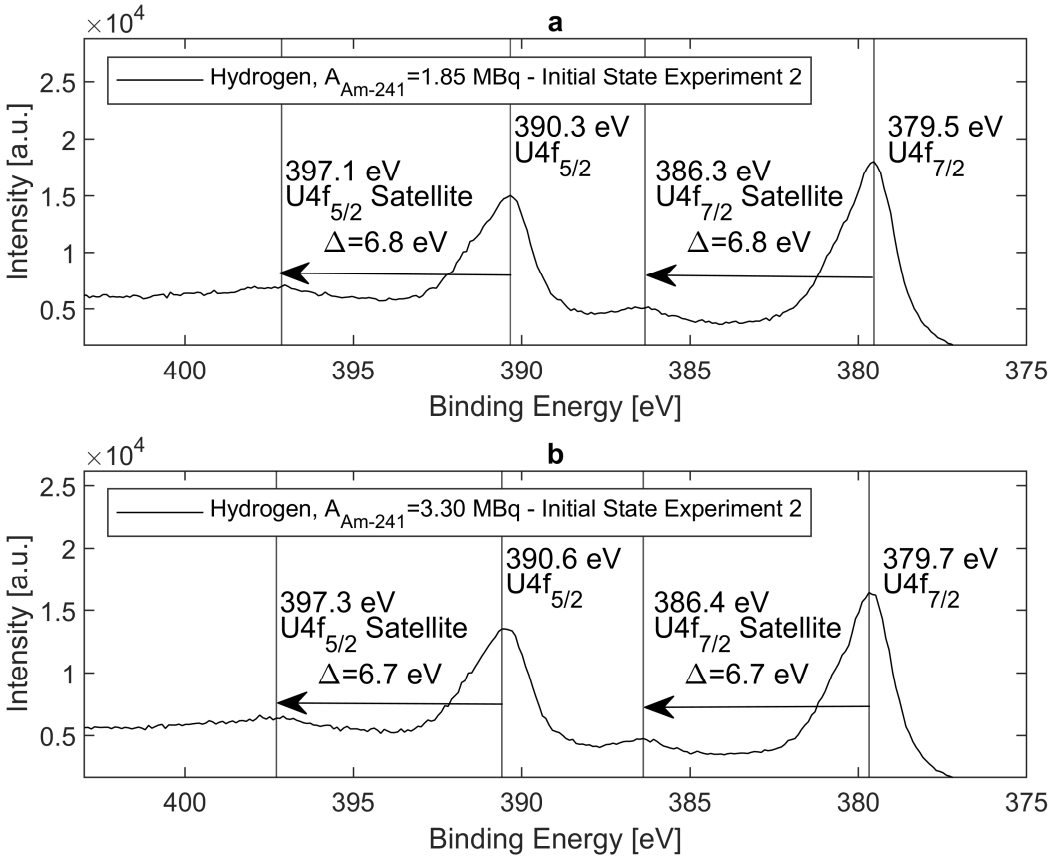


# The Influence of Hydrogen on the Radiolytic Oxidation of $UO_2$

Licentiate thesis

Niklas L. Hansson

Department of Chemistry and Chemical Engineering
CHALMERS UNIVERSITY OF TECHNOLOGY
Gothenburg, Sweden 2020

THESIS FOR THE DEGREE OF LICENTIATE OF ENGINEERING

# The Influence of Hydrogen on the Radiolytic Oxidation of $UO_2$

Niklas L. Hansson


Department of Chemistry and Chemical Engineering
CHALMERS UNIVERSITY OF TECHNOLOGY
Göteborg, Sweden 2020

The Influence of Hydrogen on the Radiolytic Oxidation of $UO_2$
NIKLAS HANSSON

© NIKLAS HANSSON, 2020

Licentiatuppsatser vid Institutionen för Kemi och Kemiteknik
Chalmers tekniska högskola
Ny serie Nr 2020:01

Department of Chemistry and Chemical Engineering
Chalmers University of Technology
SE-412 96 Gothenburg
Sweden
Telephone +46 (0)31-772 1000

Cover: Initial U4f-spectra of the $UO_2$ pellets after their carbonate washing procedure and prior to exposure to the (a) 1.85 MBq and (b) 3.30 MBq Am-241 sources under $H_2$ atmosphere.

Printed by:
Chalmers Reproservice
Gothenburg, Sweden 2020

# The Influence of Hydrogen on the Radiolytic Oxidation of $UO_2$

NIKLAS HANSSON

Nuclear Chemistry
Department of Chemistry and Chemical Engineering
Chalmers University of Technology

**Abstract**

Spent nuclear fuel from the nuclear fuel cycle contains radiotoxic nuclides which must be safely stored for over 100 000 years. The Swedish final repository concept, KBS-3, is based on engineered and geological barriers that prevent the nuclear fuel from coming in contact with groundwater, which is the most credible vector to transport the radionuclides into the biosphere. In the safety assessment of a repository, the water intrusion scenario must therefore be investigated.

The $UO_2$ matrix contains the majority of the long-lived radiotoxic elements. As the U(IV) form is highly insoluble, the release of the radiotoxic nuclides is largely governed by oxidation of the $UO_2$ matrix into the much more soluble U(VI) form. Oxidation can occur due to the formation of radiolytic oxidants through the ionization or excitation of water molecules in contact with fuel.

Oxidation of $UO_2$ pellets using external Am-241 sources was studied under conditions where the $UO_2$ surface and the source were separated by 30 µm water. $H_2$ was shown to suppress the surface oxidation as well as dissolution. This was shown by direct measurement of the surface oxidation state using XPS, as well as through concentration measurements in solution using mass spectrometry (ICP-MS).

Oxidative dissolution of 10 and 24 wt% Pu-doped MOX pellets was also studied under Ar and $D_2$ atmospheres. The $D_2$ atmosphere suppressed the uranium dissolution. However, corrosion of the stainless-steel materials present in the autoclave system was also observed. A calculation model was also developed for calculating dose-rates from α-doped $UO_2$ based material.

**Keywords**: $UO_2$, Radiolytic Oxidation, XPS, Hydrogen Effect, MOX, Dose-Rate

## List of Papers

This thesis is based on the following papers or manuscripts:

**Paper I**

**N.L. Hansson**, P.L. Tam, C. Ekberg, K. Spahiu, *XPS study of external α-radiolytic oxidation of $UO_2$ in the presence of argon or hydrogen*, Manuscript.

**Paper II**

**N.L. Hansson**, C. Ekberg, K. Spahiu, *Alpha Dose Rate Calculations for $UO_2$ Based Materials using Stopping Power Models*, Nuclear Energy and Materials, Accepted Nov 2019

**Paper III**

L. Bauhn, **N.L. Hansson**, C. Ekberg, P. Fors, R. Delville, K. Spahiu, *The interaction of molecular hydrogen with α-radiolytic oxidants on a (U, Pu)$O_2$ surface.* Journal of Nuclear Materials, 2018. **505**: p. 54-61.

**Paper IV**

L. Bauhn, **N.L. Hansson**, C. Ekberg, P. Fors, K. Spahiu, *The fate of hydroxyl radicals produced during $H_2O_2$ decomposition on a SIMFUEL surface in the presence of dissolved hydrogen.* Journal of Nuclear Materials, 2018. **507**: p. 38-43.

## Contribution report

**Paper I** – Main part of the experimental work, writing and data evaluation.

**Paper II** – All of the experimental work, modelling and main part of the writing.

**Paper III** – Main part of the experimental work, part of the writing.

**Paper IV** – Part of the experimental work, part of the writing.

# Table of Contents

# 1. Introduction

Nuclear power has seen a resurgence in recent years with over 50 reactors currently under construction in 16 countries [1] and six consecutive years of increase in electricity production [2]. The resurgence is largely due to efforts to meet increasing energy demand, reducing fossil fuel dependence and lowering of greenhouse gas emissions. As of October 2019, nuclear power constituted 10.3% of the global electricity production [3], and ~40% of the electricity production in Sweden. In the process of generating electricity from nuclear power, long-lived and highly radioactive waste products are formed which must be stored safely for extensive time periods to prevent long-lived radiotoxic nuclides from spreading in the environment. Because of the long half-lives of the actinides, the required time period in the final repository is roughly 100 000 years before the activity has reached that of the natural uranium used to manufacture the nuclear fuel. In order to ensure the stability of the repository under these geological time periods, a number of engineered and natural safety barriers will be in place. However, the safety of such a repository is regarded to be one of the main challenges of nuclear power.

In Sweden there are plans to construct a final repository at a depth of ~500 m in the granitic bedrock using the KBS-3 design developed by the Swedish Nuclear Fuel and Waste Management Company, SKB. This is the most developed repository concept globally and is already under construction by the Finnish waste management company Posiva at the Olkiluoto reactor site [4]. In this design, the fuel rods are stored in iron inserts that are contained in copper canisters which in turn are surrounded by compacted bentonite clay in the granitic bedrock. These barriers are designed to prevent groundwater from coming in contact with the fuel. Nevertheless, the most credible vector in transporting the radionuclides into the biosphere is the groundwater, and the intrusion scenario must be thoroughly investigated as part of the safety analysis [5]. In this scenario, water leaking into the damaged copper canisters comes into contact with the iron inserts and fuel rods. The strong radiation field of the spent nuclear fuel in contact with the groundwater causes substantial water radiolysis, producing high amounts of radiolytic oxidants. These oxidants can alter the oxidation state of the $UO_2$ matrix and turn the sparsely soluble U(IV) into the many orders of magnitude more soluble U(VI). However, the iron inserts corrode in contact with the groundwater, producing high pressures of hydrogen. Hydrogen has been shown to have a protective effect on nuclear fuel, preventing radiolytic oxidation.

In this work, α-radiolysis of water in contact with α-doped $UO_2$ and nuclear fuel has been modelled and experimentally studied. The influence of hydrogen on the oxidation of $UO_2$, SIMFUEL and MOX (mixed oxide $UO_2$+$PuO_2$) was also studied experimentally. The effect of hydrogen on the surface oxidation of $UO_2$ pellets using external Am-241 sources was studied using X-ray photoelectron spectroscopy.

# 2. Background

## 2.1. Uranium

Uranium is present in nature in numerous mineral types as the uranium isotopes U-234, U-235 and U-238, which have relative abundances of ~0.005%, ~0.72% and ~99.275%, respectively [6]. The principal oxidation states of uranium are U(IV), U(V) and U(VI), however, uranium can also exist in the unstable U(III) oxidation state [7]. Tetravalent uranium forms sparsely soluble compounds at pH-values ranging from mildly acidic to alkaline, as opposed to hexavalent uranium, which is highly soluble. U(V) is under many circumstances prone to disproportionation into U(IV) and U(IV) [8]. The principal pentavalent uranium ion in aqueous solution is $UO_2^+$, which disproportionates quickly, making its aqueous chemistry hard to study [9]. The hexavalent uranium naturally occurs as the linear uranyl moiety $(O=U=O)^{2+}$, which forms soluble complexes e.g. with hydroxide and carbonates [10].

## 2.2. Nuclear power

In traditional light water nuclear reactors, thermal neutron fluxes are used to fission U-235-enriched $UO_2$ fuel. The U-235 enrichment is usually in the 2-4% range to provide sufficient fissionable material to sustain a chain reaction, however other reactor designs allow for operation using slightly enriched or even natural uranium composition [11]. In the manufacturing of the fuel, $UO_2$ is pressed in the form of fine-grained powder and sintered at 1700°C into cylindrical pellets with ~95% theoretical density [12]. The pellets are stacked in Zr-alloy cladding tubes that constitute the fuel rods. These fuel rods are mounted in groups or clusters that form the fuel assemblies in the reactor core [13]. Fresh nuclear fuel is almost stoichiometric $UO_{2.001}$, however a slight increase in nonstoichiometry during reactor operation occurs [14].

The process of electricity generation through nuclear fission utilizes the enormous amount of energy that is released as the uranium nucleus is split. In the fission reaction of U-235, ~200 MeV (equivalent to $2 \cdot 10^7$ kWh·kg$^{-1}$), is released in the form of kinetic energy distributed between the emitted neutrons and fission products [10]. The fission reaction normally yields two fission products but in relatively rare events ternary fission occurs [15]. A general fission reaction of U-235 can be expressed as:

$$ {}^{1}_{0}n + {}^{235}_{92}U \rightarrow {}^{A_1}_{Z_1}FP_1 + {}^{A_2}_{Z_2}FP_2 + x\,{}^{1}_{0}n + energy \quad (1) $$

where x is ~2.5 [16]. The fission yield distribution has peaks for $FP_1$ and $FP_2$ around mass numbers 97 and 137, respectively [17]. These fission products constitute the major part of the radiotoxicity on short time scales, up to approximately 100 years, during which time period the waste is the most hazardous. Actinides are also disposed to undergoing neutron capture reactions:

$$ {}^{1}_{0}n + {}^{A}_{Z}X_1 \rightarrow {}^{A+1}_{Z}X_2 + \gamma \quad (2) $$

producing heavier actinides through the subsequent $\beta^-$-decay of $X_2$. This leads to the production and accumulation of different isotopes of e.g. plutonium and americium. These elements are

radiotoxic, have half-lives up to the order of a millions years and constitute the principal part of the radiotoxicity of spent nuclear fuel under the geological time scales considered in a final repository. The radiotoxicity of the actinides and fission products in typical spent nuclear fuel with 4% enrichment and 45 MWd/kg burnup was modelled by Holm and can be seen as a function of time in Figure 1 [18].

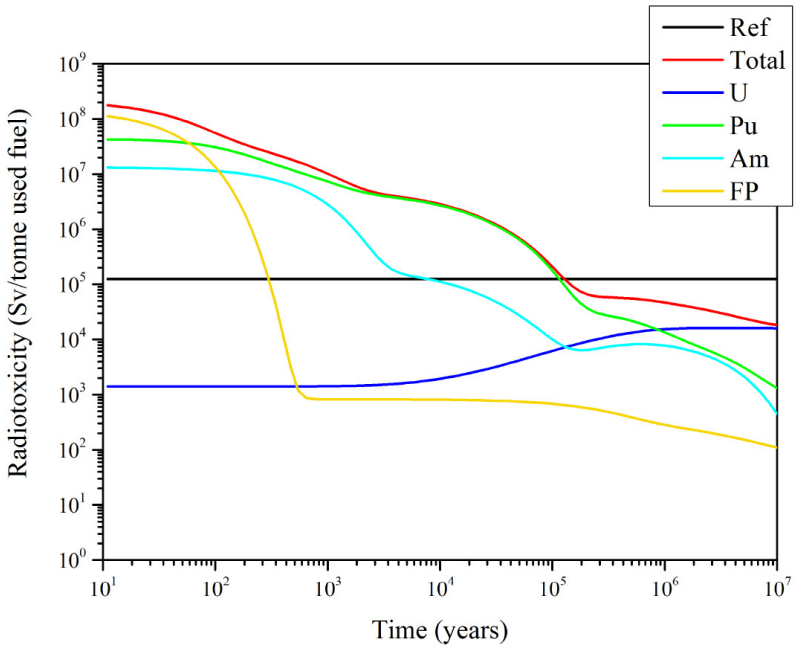


*Figure 1 - Radiotoxicity of spent nuclear fuel with 4% enrichment and 45 MWd/kg burnup as a function of time. The contributions of different actinide elements and fission products are shown separately [18]. The reference level corresponds to the radiotoxicity of the mined uranium.*

## 2.3. Fission products

The fission products have varying degrees of solubility in the $UO_2$-matrix and can be categorized accordingly in terms of decreasing solubility [12, 19]:

1. Fission products, actinides and lanthanides that are soluble in the $UO_2$-matrix. This category constitutes the vast majority of radionuclides >90%.
2. Fission products that migrate to the grain boundaries, forming either metallic ε-particles consisting of Mo, Ru, Rh, Tc and Pd or perovskite phases in the form of $(Ba/Sr)ZrO_3$. However, not all of the Zr is precipitated in the perovskite phase, as 25% is dissolved in the $UO_2$-matrix [19].
3. Volatile radionuclides that migrate to the fuel gap, e.g. the fission gases Ar, Kr and Xe, and to a lesser extent Cs and I.

The volatile species belong to what is called the instant release fraction [20], and are released to a significant degree at the moment of water intrusion into the canister. The species that are dissolved in the form of a solid solution in the $UO_2$ matrix (e.g. $PuO_2$, which forms an almost ideal solid solution) have a dissolution rate that is governed by the dissolution rate of the matrix itself.

## 2.4. Final repository

Radioactive waste is divided into different categories according to its initial level of radioactivity and decay rate. These categories are low-, intermediate- and high-level waste, which are additionally subcategorized as short- or long-lived [21]. SKB divides these into three main combined categories: low- and intermediate-level long-lived waste, low- and intermediate-level short lived waste and high-level long-lived waste. Waste in these three categories will be sent to different repositories designed for the handling of the specific waste. Spent nuclear fuel is sorted into the high-level long-lived waste category. The safety design of the repository meant for the storage of this waste category is considerably more demanding than the ones in the other categories, as it is hard to predict conditions for any site over geological time scales [21].

The long term behaviour of $UO_2$ and actinides can be better understood by studying their behaviour in nature. The best long-term radionuclide migration data that exists is from the natural nuclear reactor sites that existed in Oklo, Gabon approximately two billion years ago [22]. These natural reactor sites are often used as a natural analog of spent fuel behaviour in the environment [23]. The reactors were critical intermittently, in cycles of evaporating and regaining moderator, for a period of a few to several hundred thousand years. The Oklo scenario is applicable for a variety of candidate host rocks, as several different mineral types were present at the Oklo reactor sites [22]. In studies of the radionuclide migration, the actinides, and to a large extent the fission products, were retained in the host rock close to their formation site [22]. Therefore, the construction of a repository in crystalline bedrock is considered a highly suitable alternative for the long-term storage of spent nuclear fuel.

The KBS-3 final repository concept is designed to safely store all of the high-level long-lived waste produced in Sweden at the Forsmark SR-Site. The repository will be built at a depth of approximately 500-700 m in the crystalline bedrock using a tunnel structure, which is backfilled after the canisters are positioned. After approximately 100 000 years, the radiotoxicity of the fuel in the repository will have reached the level of the uranium ore used in the fuel production [5]. The safety barriers in the Swedish KBS-3 design include the crystalline bedrock, bentonite clay, the copper canister with an iron insert, as well as the fuel pellet and cladding tube. At the 500-700 m depth of a final repository, the conditions are reducing due to the consumption of oxidizing species through reactions with minerals and organic material, and oxygen partial pressures can be approximated as zero. Studies of oxygen consumption of the potentially confined oxygen in the vault have shown that completely anoxic conditions are likely reached within 670 years at a temperature of 75 °C only through reactions with the copper canister [24].

The principal mechanism for the release of radiotoxic nuclides from the canister is through the failure of the structural integrity of the canister, followed by groundwater intrusion. The scenarios leading to a water-filled canister in the repositories long term evolution are discussed in SKB's main safety assessment report of the SR-Site project [5]. The main risk-contributing scenarios discussed in the report are:

a) Canister failure due to shear load (in case of a large earthquake in the vicinity of the repository).
b) Canister failure due to corrosion (for advective conditions in the bentonite buffer, assumed to be caused by buffer erosion).

The direct contact of water with the fuel bundles leads to the release of the instant release fraction [20], which occurs without oxidative dissolution of the $UO_2$ matrix. However, the elements that are dissolved in the fuel matrix (or exist at grain boundaries) require oxidizing conditions to be released, as the solubility of the $UO_2$-matrix in the U(IV) oxidation state is low [25]. Therefore, the dissolution is entirely dependent on the oxidation of the nuclear fuel into the many orders of magnitude more soluble U(VI) state. This can occur through the formation of locally oxidizing conditions through water radiolysis. As the canister breach scenario is unlikely to occur before 1000 years after closing of the repository, the α-radiation will be the dominant constituent of the radiation field.

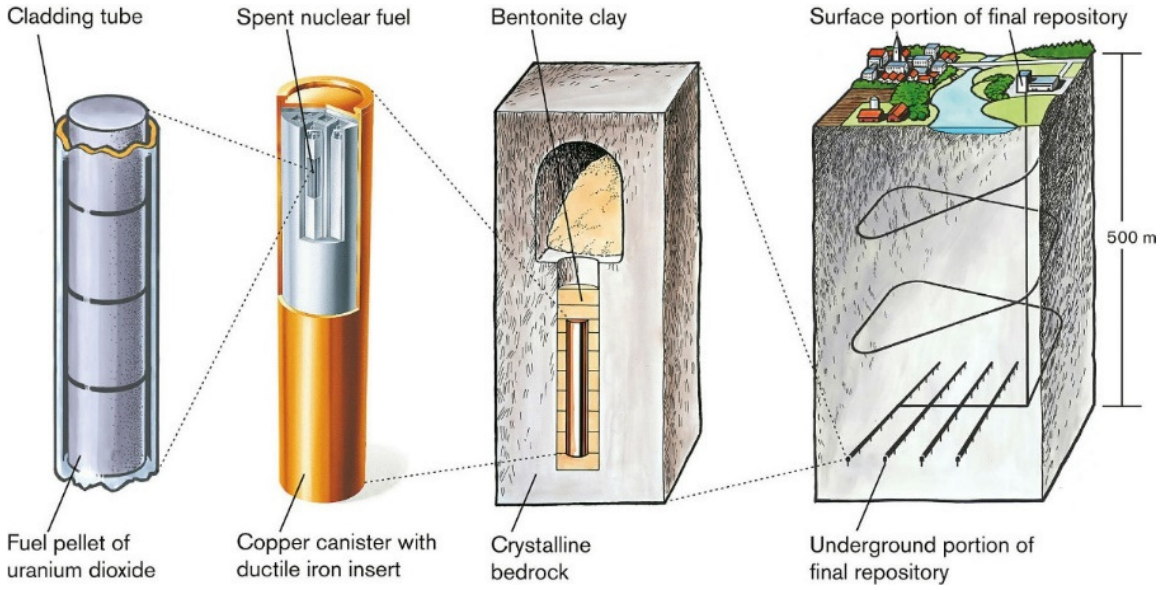


*Figure 2 - The KBS-3 design with the fuel pellet, copper canister, bentonite clay and crystalline bedrock safety barriers. Illustration: Jan Rojmar, Svensk Kärnbränslehantering AB.*

# 3. Theory

## 3.1. Radiolysis

Radiolysis is the ionization or molecular dissociation due to interaction with ionizing radiation. In water, the energy from radioactive decay leads to an excitation of water molecules into the excited $H_2O^*$ state or direct ionization into the $H_2O^+$ ion. The primary interaction occurs during $<10^{-16}$ s after exposure, which corresponds to the time period of an electronic transition. The ionized $H_2O^+$ ions react with water molecules, producing $H_3O^+$ and hydroxyl radicals, $\cdot OH$, ($<10^{-14}$ s after exposure). The excited $H_2O^*$ molecule primarily splits into the $H\cdot$ and $\cdot OH$ radicals ($\leq 10^{-13}$ s) [26]. These radicals can subsequently recombine, leading to the formation of molecular products such as $O_2$, $H_2$ and hydrogen peroxide, $H_2O_2$. The result is a variety of products, of which there are both oxidizing and reducing species. A generalized reaction of α-radiolysis of water can be seen in Eq. 3.

$$H_2O \xrightarrow{\alpha} H^+, H\cdot, e^-_{aq}, HO_2\cdot, \cdot OH, OH^-, H_2, O_2, H_2O_2 \quad (3)$$

Radiolysis yields are often expressed in terms of G-values for the specific media and type of radiation, in units: moles produced per Gy (J/kg) absorbed radiation. Since α-radiation has a high linear energy transfer (LET), the radicals formed in the particle track are more likely to recombine into molecular products, and the molecular yields (G-values) are therefore higher than under β- and γ-radiolysis [27]. As the reducing molecular hydrogen is chemically inert under the temperatures relevant to the repository, the net effect of radiolysis will be oxidizing without chemical activation of $H_2$ [28]. In the case of radiolytic oxidation of $UO_2$, $H_2O_2$ is the dominant oxidant under α-radiolysis, with a very high relative impact [29]. However, recent reports have shown that $H_2O_2$ dissociates to a large extent on the surface of $UO_2$ doped with metallic particles, such as in the case of SIMFUEL [30, 31], thereby increasing the importance of $O_2$ as an oxidant. Additionally, under radiation fields (especially β- and γ- fields), the presence of environmental $O_2$ can greatly increase the radiolytic production of oxidants [12].

## 3.2. Dose-rate and radiolytic production

The production of radiolytic oxidants in water that is in contact with nuclear fuel is an important parameter in the safety assessment of the water intrusion scenario. In order to model the production of radiolytic oxidants, the attenuation of the radiation in the $UO_2$-matrix has to be calculated. In this calculation, the crucial parameter is the mass stopping power ($MeV\cdot cm^2\cdot g^{-1}$) of the particles in the media. Most stopping power models are based on the Bethe-Bloch equation, which describes the attenuation of a charged particle due to electromagnetic interactions in the target material [32, 33]. The stopping power spectrum is commonly divided into the low-, medium- and high-speed regimes, respectively [34]. The Bethe-Bloch equation with shell and density effect corrections can accurately describe the attenuation of a particle in the high-speed regime. However, the α-particle energy spectrum of nuclear fuel is typically in the 5 MeV energy range and is not well described by the Bethe-Bloch equation, as the model has discrepancies with experimental data in the <1

MeV/nucleon (4 MeV α-particles) energy range [35]. Therefore, theoretical models that are normalized using experimental data are generally used to describe α-particle attenuation in the low energy regime. Such mass stopping power data can be found in the ASTAR and SRIM databases.

The calculation model is described in detail in Paper II [36], and will only be described briefly in this section. The emitted α-particles can be considered to only be emitted in the depth interval [0, $\delta_{max}$], where $\delta_{max}$ is the maximum range of an α-particle in the material. The polar emission angle can be described in the interval [0, π/2], where 0 is perpendicular to the modelled surface. As the emission angle interval [0, -π/2] is symmetrical with the considered interval, it can be omitted. Similarly, particles emitted inwards will not escape the $UO_2$-matrix, and the interval [π/2, π] is omitted in the model. The particles are attenuated in a stepwise manner along the path length with a step size s=0.01 µm. The spherical coordinate system can be simplified by acknowledging that the azimuthal emission angle φ yields a symmetrical emission path with φ=0. Additionally, the dimensions of a $UO_2$-pellet are significantly larger than the maximum particle range in the material, which makes the curvature negligible. The system can therefore be simplified as a planar geometry. The resulting simplified coordinate system is shown in Figure 3.

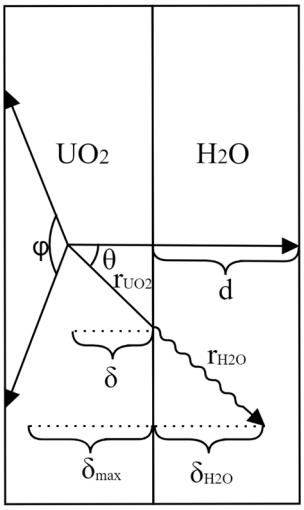


*Figure 3 - The planar coordinate system used to illustrate the model geometry.*

## 3.3. Anoxic corrosion of iron

In the water intrusion scenario, significant corrosion of the massive iron inserts occurs, forming iron hydroxide and magnetite ($Fe_3O_4$), as shown in reactions 4 & 5, respectively [37, 38]:

$$Fe + 2H_2O \rightleftarrows Fe(OH)_2 + H_2 \quad (4)$$

$$3Fe + 4H_2O \rightleftarrows Fe_3O_4 + 4H_2 \quad (5)$$

The reactions are thermodynamically favorable even under anoxic conditions with high hydrogen equilibrium pressures [37]. The resulting pressure in the repository due to the iron corrosion reactions is estimated to be ≥50 bar, which is equivalent to the relevant repository hydrostatic

pressure [28]. The presence of the reducing species Fe(II) in a solid phase or dissolved species (through reactions 4 & 5) can cause consumption of the strong oxidants such as $H_2O_2$, through the reaction:

$$Fe(II) + H_2O_2 \rightleftarrows Fe(III) + OH\cdot + OH^- \quad (6)$$

causing the consumption of both species [39]. The presence of Fe(II)-containing solid phases can also directly cause reduction of oxidized U(VI). This effect will likely have a significant impact on the safety of a nuclear repository under the water intrusion scenario, as indicated in several studies [40, 41].

## 3.4. Hydrogen effect

Significant amounts of molecular hydrogen are produced through the anoxic corrosion of iron, and to a much lesser extent through radiolysis of water. Molecular hydrogen has in several studies been shown to protect the fuel surface from radiolytic oxidation [42]. The main mechanism in studies of nuclear fuel is through the kinetic activation of the hydrogen on catalytic metallic ε-particles, which consist of Mo, Tc, Ru, Rh, Pd solid solutions [43]. The hydrogen activation occurs through the interaction and breaking of the hydrogen-hydrogen bond, which is well described in the case of interactions with transition metals [44]. The activated hydrogen is reactive and can reduce oxidized uranium or consume oxidizing species. However, molecular hydrogen has been shown to influence the oxidative dissolution in studies, even in the absence of ε-particles, but the underlying mechanism is not fully understood. In a study by Bauhn et. al., where homogeneous oxidation of highly active Pu-238 solutions was studied, it was shown that the hydrogen effect was not present in the absence of an activation surface in the form of $PuO_2$ [45]. In another study by Carbol et. al. where $UO_2$ doped with 10% U-233 was studied in solution under $H_2$ atmosphere, the dissolved uranium concentration stabilized around $9\cdot10^{-12}$ M [42]. This is significantly below the solubility of $UO_2$(am), indicating that $H_2$ was activated on the $UO_2$ surface, suppressing its dissolution.

## 3.5. Uranium system

$UO_2$ exists in both amorphous and crystalline forms. Neck and Kim have studied the solubilities of the $UO_2$(am) and reviewed data for $UO_2$(cr) phases and reported the solubilities $\log_{10}K_{sp,Am}$=-54.5±1.0 and $\log_{10}K_{sp,Cr}$=-60.6±0.5 [25]. Using the hydrolysis stability constants measured by Neck and Kim (accepted in the review of Ekberg and Brown [46]), the solubilities of the $UO_2$(am) and $UO_2$(cr) phases can be calculated as function of pH.

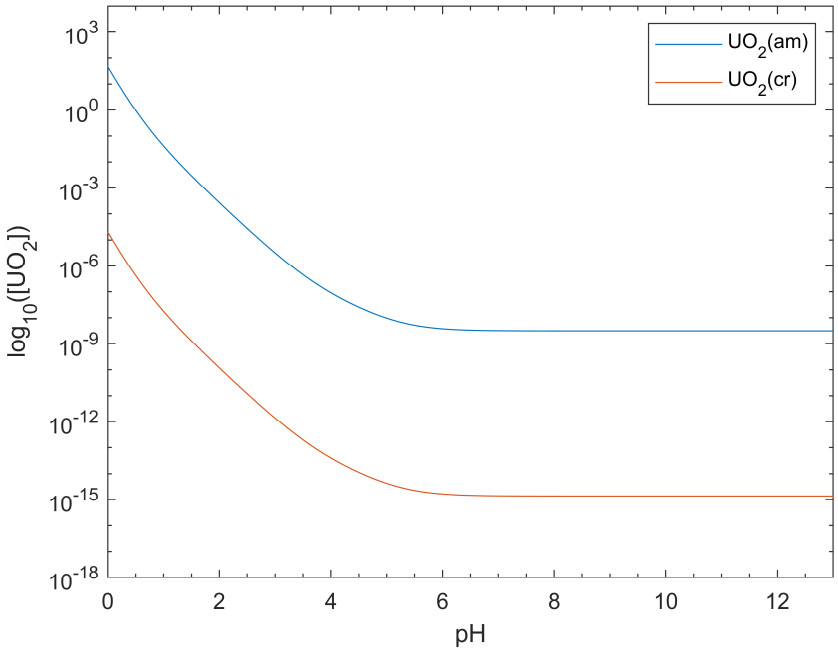


*Figure 4 - Solubilities of $UO_2$(am) and $UO_2$(cr) using the data from Neck and Kim [25].*

## 3.6. Oxidative dissolution

### 3.6.1. Conductivity

The dissolution kinetics are highly dependent on the solid-state conductivity, as the rate-controlling step is the transfer of a charge to the oxide surface, where ionic species can be released into solution. Stoichiometric $UO_2$ is a p-type semiconducting oxide with low conductivity. As it is oxidized to $UO_{2+x}$, U(V) and/or U(VI) create holes in the U5f sub-band. These holes can migrate, giving rise to moderate conductivity. Oxidized $UO_{2+x}$ has been shown to catalyze the $O_2$ reduction as well as decomposition of $H_2O_2$, as the more conductive $UO_{2+x}$ can enable charge transfers required for the redox reactions [47].

### 3.6.2. Corrosion

The oxidation of $UO_2$ can be viewed as a corrosion process, where the anodic reaction is the oxidation and dissolution of the fuel coupled with the cathodic reaction, which is the reduction of the oxidizing species. The cathodic and anodic reactions can be expressed as:

$$UO_2 \rightarrow UO_2^{2+} + 2e^- \quad (7)$$

$$Ox + 2e^- \rightarrow Red \quad (8)$$

respectively [12]. As the solubility of uranium is highly dependent on its oxidation state, the process is significantly influenced by the redox potential in solution. Uranyl ($UO_2^{2+}$) starts dissolving already at very low potentials (-300 mV vs SCE) in neutral and alkaline pH solutions.

### 3.6.3. Final repository conditions

In the KBS-3 final repository design, the conditions at a depth of ~500-700 m will be reducing. All the initially present oxidizing species are in due course consumed under the repository conditions through reactions with minerals, organic material and the copper canister. The $E_h$ value will therefore tend towards the $H_2O/H_2$ potential. Under these conditions the $UO_2$-phase is highly stable. Under water radiolysis, strong oxidants with redox potentials (i.e. $E_{OX/RED}$) that are significantly higher than the equilibrium potential of the $UO_2^{2+}/UO_2$ pair ($E_{UO2^{2+}/UO2}$) will be produced. Under these conditions, a corrosion potential, $E_{CORR}$, will be established at the fuel surface-liquid interface that will depend on the kinetics of the cathodic and anodic reactions (Eq. 7 & 8). Grain boundaries can contain local hyper-stoichiometries of $UO_{2+x}$, which can enhance the reactivity and dissolution [48]. The oxidation of $UO_{2+x}$ also shrinks the unit cell parameter slightly, causing a weakening of the grain boundary [48]. Fission products that gather at the grain boundaries therefore are at a higher risk of release due to oxidative dissolution.

### 3.6.4. Oxidative dissolution threshold

The anodic oxidation of $UO_2$ in neutral to alkaline conditions has been observed in many studies to proceed in steps: $UO_2 \rightarrow UO_{2+x} \rightarrow UO_2^{2+}(aq) \rightarrow UO_3 \cdot yH_2O$, where $UO_3 \cdot yH_2O$ is schoepite [12]. Schoepite can be deposited on the $UO_2$ surface, which can hinder further oxidation [49]. In the process of oxidizing $UO_2$ to $UO_{2+x}$, $O^{2-}$ is injected into interstitial sites in the fluorite structure, causing neighboring U(IV) to oxidize to U(V) or U(VI) to maintain charge neutrality. The threshold where the oxidative dissolution is significantly increased has been thoroughly investigated and has been found to be at $UO_{2.33}$ [50]. The anodic dissolution of $UO_{2.33}$ can be expressed as:

$$UO_{2.33} + 0.33\, H_2O \rightleftarrows UO_2^{2+} + 0.66\, OH^- + 1.34\, e^- \quad (9)$$

$$xUO_2^{2+} + yH_2O \rightleftarrows (UO_2)_x(OH)_y^{(2x-y)+} + yH^+ \quad (10)$$

### 3.6.5. Intermediate oxides

Under normal aerated conditions, the equilibrium potentials for the formation of $U_4O_9$, $U_3O_7$, $U_3O_8$ and $UO_3 \cdot yH_2O$ are considerably lower than the $E_{CORR}$ value [12]. Aerated conditions can therefore lead to a complex combination of oxides on the fuel surface. Leinders et. al. and Kvashnina et. al. studied the uranium oxidation states of the intermediate oxides between $UO_2$ and $UO_3$ using HERFD-XANES [51, 52]. The researchers identified the uranium oxidation states in the intermediary phases as:

- $U_4O_9$: 2·U(IV) + 2·U(V)
- $U_3O_7$: U(IV) + 2·U(V)
- $U_3O_8$: 2·U(V) + U(VI)

The oxidative dissolution threshold of $UO_{2.33}$ therefore corresponds to the dissolution of a U(IV)- and U(V)-containing phase, and not of a U(VI)-containing phase. However, any oxidation above this state would include a U(VI) component. The transition from $U_3O_7$ to $U_3O_8$ involves a significant increase in lattice volume by ~30% as the material transitions from a fluorite type

structure to a layered one [53]. This transition occur as the material goes from a combination of the oxidation states U(IV)+U(V) to a combination of U(V)+U(VI) [51].

### 3.6.6. Influence of pH

The anodic dissolution of oxidized uranium (Eq. 10) results in a decrease in pH, which increases the dissolution rate of $UO_2^{2+}$, relative to neutral conditions. The reaction (Eq. 10) occurs at a very high rate under highly positive potentials, (>300 mV vs SCE) [12], able to cause acidic conditions locally, e.g. in occluded sites. At these sites, the acidic conditions can be maintained by being protected from convection into the bulk solution. At pH below 5, the $UO_{2.33}$ layer is not observed on the surface, as it is dissolved very efficiently. Low pH also fully prevents the formation of schoepite on the surface, the presence of which can inhibit further oxidation [49].

## 3.7 Groundwater systems

### 3.7.1. Carbonate system

Carbonate is present in most groundwater models relevant to the water intrusion scenario. In Swedish ground water, the concentration of carbonate is 2-10 mM [54]. The carbonate concentration is dependent on the calcium concentration present in the groundwater, as $CaCO_3$ is ubiquitous and has a solubility product of $(5.25\pm0.65)\cdot10^{-4}$ M at 25°C [55]. The presence of carbonate has a significant influence on the dissolution rate of oxidized uranium, as it forms strong soluble complexes with the uranyl ion. The dissolution rate of $UO_{2.33}$ is roughly $4.8\cdot10^{-6}$ $g\cdot cm^{-2}\cdot d^{-1}$ in 10 mM carbonate solution, compared to $1\text{-}9\cdot10^{-8}$ $g\cdot cm^{-2}\cdot d^{-1}$ in the much more inert perchlorate solution [56]. The carbonate system is the equilibria between the different forms $H_2CO_3$, $HCO_3^-$ and $CO_3^{2-}$.

$$H_2CO_3 \rightleftarrows HCO_3^- \rightleftarrows CO_3^{2-} \tag{11}$$

with $pK_1$=6.35 and $pK_2$=10.33 at 25°C [57]. At neutral to slightly alkaline pH, which is the relevant region for the groundwater considered in the water intrusion scenario, the $HCO_3^-$ form is dominating. In closed systems where $HCO_3^-$ is the dominant conjugated acid and base, the pH will stabilize approximately between $pK_1$ and $pK_2$, i.e. pH ~8.3. However, under conditions where $K_2[HCO_3^-]$ is not significantly larger than $K_w$, i.e. for concentrations of approximately $[HCO_3^-]<3$ mM, the pH will be somewhat dependent on $[HCO_3^-]$.

### 3.7.2. Calcium carbonate system

In seawaters, the speciation of uranyl in the presence of carbonate was previously estimated to be dominated by the $UO_2(CO_3)_3^{4-}$ and $UO_2(CO_3)_2^{2-}$ complexes, with relative abundances of 97% and 3%, respectively [58, 59]. However, in this estimation, the influence of calcium was neglected, despite the fact that calcium is ubiquitous in groundwater and seawater. Calcium can influence the speciation through the formation of the complexes $CaUO_2(CO_3)_3^{2-}$ ($\log \beta_{113} = 27.2\pm0.5$) and $Ca_2UO_2(CO_3)_3$ ($\log \beta_{213} = 30.7\pm0.5$) [60-63]. In a more recent study by Endrizzi and Rao, the effect of calcium was taken into account, which showed that the dominant complex under seawater

conditions was the neutral $Ca_2UO_2(CO_3)_2$ complex [59]. This is also true in the case of natural groundwaters [64].

The presence of a solid Fe(II)-containing phase can reduce U(VI), causing precipitation of reduced U(IV) due to its low solubility. Uranyl also adsorbs efficiently on iron oxides and hydroxides, both of which can exist in the form of minerals or clay skins in sediments. The adsorption is however negatively correlated with calcium concentration in carbonate-containing solutions, suggesting that the formation of $CaUO_2(CO_3)_3^{2-}$ and $Ca_2UO_2(CO_3)_3$ limits the adsorption of uranyl on mineral surfaces [64]. The same complexes can potentially prevent the reduction and precipitation on metallic iron or Fe(II)-containing mineral surfaces.

## 3.8. X-ray photoelectron spectroscopy

### 3.8.1. Principles of XPS

X-ray photoelectron spectroscopy (XPS) is a nondestructive measurement technique that utilizes the photoelectric effect [65]. X-rays with high frequency and energies typically in the ~1 keV range are fired at a surface under high or ultra-high vacuum ($10^{-8}$ or $10^{-9}$ mbar, respectively). This causes ejection of atomic core electrons, which are subsequently measured with energies corresponding to their binding energy. The electron binding energies of the atom are dependent on the chemical environment, and can therefore be used to analyze the chemical state of a material [66].

### 3.8.2. XPS measurements of U4f

The positions of the U(IV) and U(VI) components of the $U4f_{7/2}$-peak in the XPS-spectra have been reported by a number of authors as approximately 380 and 382 eV, respectively [14, 67-69]. The main method of uranium oxidation analysis using XPS is by measuring the U4f region, after which the $U4f_{7/2}$-peak is deconvoluted into its U(IV), U(V) and U(VI) states. Complementary analysis in the form of satellite peak positions and valence band analysis can also be performed [50].

# 4. Materials and Methods

## 4.1 Pellets and radiation sources

### 4.1.1. $UO_2$ pellets

Pellets consisting of 99.3% $^{238}U$ and 0.7% $^{235}U$, as well as slightly enriched pellets consisting of 98.0% $^{238}U$ and 2.0% $^{235}U$, were used. The 2 wt% enriched pellets have $2.64 \cdot 10^4$ Bq/g specific α-activity.

### 4.1.2. MOX pellets

The 24 wt% Pu-doped unirradiated mixed oxide $UO_2$ + $PuO_2$ (MOX) pellet was produced in 2006 at Belgonucleaire in Belgium through the Micronized Masterblend (MIMAS) process. A 93.0% theoretical density was achieved, with a grain size of roughly 7 µm. The specific α-activity was determined as 4.96 GBq/g. Americium content was measured using gamma spectrometry, determined as 77.8 µg/g. Carbon was also measured using a thermal conductivity technique, and was determined to be 37 ppm wt. A 1.302g half-cylinder slice of the pellet with a geometrical surface area ($S = \pi r^2 + r\pi h + 2rh$) of 1.597 $cm^2$ was used in the experiments. For further details about the production and characterization of the 24 wt% Pu-doped MOX pellet, see [70]. The calculated isotopic composition of the pellet can be seen in Table 1.

*Table 1.* Calculated composition and dimensions of the 24 wt% Pu-doped MOX piece (updated 2019-07-19).

| Oxide composition | | | Pu/Am isotopic composition | | Dimensions | |
|---|---|---|---|---|---|---|
| $UO_2$ | $PuO_2$ | $AmO_2$ | **June 2019** | | Diameter | Height |
| 75.11 wt% | 23.61 wt% | 1.29 wt% | $^{238}Pu$ | 2.06% | 8.73 mm | 4.43 mm |
| | | | $^{239}Pu$ | 55.09% | | |
| | | | $^{240}Pu$ | 25.91% | | |
| | | | $^{241}Pu$ | 4.82% | | |
| | | | $^{242}Pu$ | 6.96% | | |
| | | | $^{241}Am$ | 5.17% | | |

Additionally, two cylindrical MOX pellets with 10 wt% Pu-doping were used in the autoclave experiments, with a theoretical density of ~95% and specific activity of 1.72 GBq/g. The pellets are unirradiated and were produced through the MIMAX MOX process in the MELOX factory, France. The pellets represent the α-radiation field of a high burnup MOX fuel after ~60 years of decay. The isotopic composition of the pellets can be seen in Table 2. The pellets have a heterogeneous microstructure with three distinct phases with different degrees of Pu-content. Additional characterization of the pellets and their phases can be found in the work of Odorowski et. al. [71].

*Table 2.* Composition and dimensions of the 10 wt% Pu-doped MOX pieces (updated 2019-07-19).

| Oxide composition | | | Pu/Am isotopic composition | | Dimensions | |
|---|---|---|---|---|---|---|
| $UO_2$ | $PuO_2$ | $AmO_2$ | **June 2019** | | Diameter | Height |
| 89.76 wt% | 10.23 wt% | 0.01 wt% | $^{238}Pu$ | 1.32% | | |
| | | | $^{239}Pu$ | 64.37% | 8.08 mm | 4.22 mm |
| | | | $^{240}Pu$ | 26.60% | 8.08 mm | 3.27 mm |
| | | | $^{241}Pu$ | 2.54% | | |
| | | | $^{242}Pu$ | 5.05% | | |
| | | | $^{241}Am$ | 0.12% | | |

### 4.1.3. SIMFUEL pellet

The SIMFUEL pellet used in this work consisted of $UO_2$ with Sr, Y, Zr, Mo, Ru, Rh, Pd, Ba, La, Ce and Nd additions in proportions analogous to 50 MWd/kg burnup fuel. The pellet was manufactured by AECL Research, Chalk River laboratories and further information can be found in [72].

### 4.1.4. Am-241 sources

Am-241 sources in the americium-oxide chemical form (Eckert & Ziegler) with α-activities 1.85 and 3.30 MBq, respectively, were used. The sources are covered by a 2 µm layer of pure gold to fix the radionuclide in the Au-matrix to prevent leakage. The dimensions of the $AmO_2$-powder compartment are Ø 15.5 x 0.4 mm. The sources are encapsulated in a SS AISI 304 frame exposing a cross-section Ø 11.5 mm.

## 4.2. Solutions and chemicals

Solutions containing NaCl, $NaHCO_3$ and $CaCO_3$ were prepared by dissolving NaCl (99.99%, Merck), $NaHCO_3$ (99.7-100.3% Sigma-Aldrich) and $CaCO_3$ (≥99.0% Sigma-Aldrich) in MQ water (18.2 MΩ).

Iron foils (≥99.99% metal basis Alfa Aesar) were used with ~0.14 g weight and 3.64 $cm^2$ surface area. A uranyl stock solution was mixed with 10 mM NaCl + 2 mM $NaHCO_3$ or 9 mM NaCl + 1.5 mM $NaHCO_3$ + 0.5 mM $CaCO_3$ solution, resulting in initial uranium concentrations of $4.5 \cdot 10^{-6}$ M and ~20 mL solution volume at the start of the experiments.

## 4.3. Instruments

### 4.3.1. XPS

A PHI5000 VersaProbe III Microprobe XPS instrument equipped with a monochromatic Al K-α X-ray source with energy 1486.6 eV [73] was used in the surface measurements. The pellets were transferred to the XPS using a PHI transfer vessel (model 04-111), which is compatible with the introduction chamber of the instrument.

### 4.3.2 Inductively coupled plasma - mass spectrometry (ICP-MS)

The uranium concentrations in solution were measured by Inductively Coupled Plasma Mass Spectrometry (ICP-MS) (Thermo Scientific iCAP Q). ICP-MS samples were prepared using 0.5 M $HNO_3$ prepared from Merck suprapur (65% $HNO_3$) and the calibration was performed using a $^{238}U$ standard in the range 0-50 ppb, with 10 ppb $^{232}Th$ as the internal standard. The detection limit is approximately 0.1 ppb using the instrument with the specified calibration method for the analyzed elements.

### 4.3.3. α-spectrometry

An Ortec, Alpha Duo, Octête α-spectrometer was used in the α-spectrometry measurements. 10 µL of the samples were mixed with an acetone-based solution (Z-100) on a planchette and were heated under an IR lamp for 10 minutes, allowing the samples to evaporate. The remaining solution was removed using a burner, leaving a very thin sample layer. The samples were placed at a close distance to the detector window to ensure a small solid angle.

### 4.3.4. UV-VIS

The $H_2O_2$-concentrations were measured spectrophotometrically at 350 nm wavelength with a Shimadzu UV-1800 using the Ghormley tri-iodide method, based on the rapid oxidation of iodide in the presence of a molybdate catalyst [74-76]. The spectrophotometer was calibrated using a 30 wt% $H_2O_2$ solution (Sigma-Aldrich). 2 mL of the samples were mixed with 100 µL 1M KI (≥99.5%, Sigma-Aldrich in MQ water) and 100 µL ammonium molybdate tetrahydrate (≥ 99.0%, Sigma-Aldrich) in an acetate buffer solution (pH 4.65, Sigma-Aldrich).

### 4.3.5. Autoclaves

Stainless-steel autoclaves (Parr Instruments Co., USA) with an internal volume of 450 mL were used. The autoclaves were equipped with stainless-steel dip tubes attached to the lid which allowed for sampling utilizing the overpressures in the autoclave experiments. The original national pipe tapered threads (NPT) connections were replaced with Vacuum Coupling Radiation (VCR) ones, making the autoclaves more leak-tight under hydrogen atmosphere at high pressures. To further ensure this, graphite gasket seals were used.

### 4.3.6. X-ray diffraction

X-ray diffraction (XRD) measurements were performed with a BRUKER D2 PHASER instrument using copper K-α lines with $\lambda_1$=1.54045 Å and $\lambda_2$=1.54439 Å. The measurements were carried out in a glove box with $p_{O2}$≤1 ppm.

# 5. Experimental

## 5.1. Alpha dose-rate calculation model

The geometrical dose-rate model was written in MATLAB 2016b. Mass stopping powers from ASTAR were obtained from the libdEdx database [35]. The ASTAR mass stopping power data is also available in the ICRU 49 report [77]. The SRIM mass stopping power data was obtained from the SRIM-2013 program. In dose-rate and range projection calculations the continuous slowing down approximation (CSDA) is widely used, which approximates the range of the particles by numerically integrating the reciprocal of the stopping power spectrum in the considered energy interval [78]. The SRIM-2013 program is equipped with the projected range algorithm (PRAL), which accounts for the curvature of the α-particle trajectory. In the calculation model, $n=10^5$ particles were generated, each with a random emission depth and polar emission angle.

The model was benchmarked using α-spectrometry, through comparison of the model to the α-spectrometric measurement. This also allowed for comparison between the different stopping power databases. The modelled fuel compositions were the 2 wt% U-235 enriched $UO_2$ pellet as well as the 10% and 24 wt% Pu-doped MOX pellet with 4.96 GBq/g specific α-activity. The dose-rates in the water layer between the Am-241 sources and $UO_2$ pellets were also modelled.

## 5.2. XPS experiment

### 5.2.1. Experimental setup

The surfaces of the pellets were polished prior to the experiments using 600 & 2400 grit SiC grinding paper to expose fresh $UO_2$ surfaces. The $UO_2$ pellets were then washed in four 80 mL $NaHCO_3$ solutions containing 50, 10, 10 and 0 mM for at least 24 h in each washing step. All work was performed in an Inert Technology Glovebox with $p_{O2} \leq 1$ ppm during the washing steps and closing of the autoclave as well as the transport vessel. All steps were performed close to room temperature (~298 K).

Experiments with $NaHCO_3$ solutions and MQ water were conducted. The $NaHCO_3$ experiments were performed in glass beakers with ~154 mL 10 mM $NaHCO_3$ under 10 bar Ar and $H_2$ atmospheres for ~45 days. The MQ experiments were performed in plastic tubes using ~45 mL MQ water under 10 bar Ar or $H_2$ atmospheres for 11 days. An additional ~154 mL MQ experiment was performed under 10 bar Ar atmosphere for 45 days to study the influence of $NaHCO_3$ on dissolution. The experimental setup was inspired by Sunder et. al. [50], who studied external oxidation of $UO_2$ pellets using Am-241 sources of strengths up to 14.8 MBq. In both the work of Sunder et. al. and in this work, the $UO_2$ pellets were separated from the Am-241 sources using a few Pyrex glass threads with 30 µm diameter placed on the gold-plated surface of the source. The experimental setup can be seen in Figure 5. The beakers and tubes containing the solutions, Am-241 sources and $UO_2$ pellets were contained in the autoclave during the experiment to ensure that the influence of the box atmosphere was minimized.

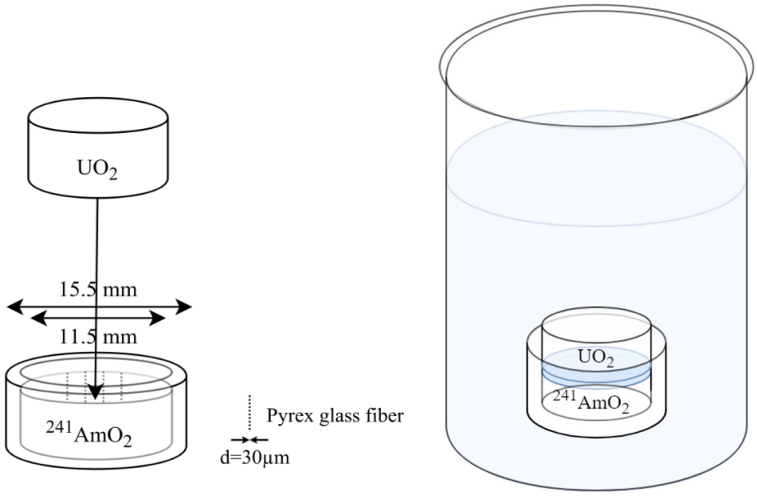


*Figure 5 – The $UO_2$-pellet placed on top of the Am-241 source with a separation of 30 µm water, achieved by placing Pyrex glass fibers in between.*

### 5.2.2 XPS analysis

The binding energy calibration was performed using the $Au4f_{7/2}$, $Ag3d_{5/2}$ and $Cu2p_{3/2}$-peaks at 83.96, 368.21 and 932.63 eV, respectively, from $Ar^+$ sputtered Au, Ag and Cu surfaces [79]. A survey scan with 1.0 eV energy step size was first performed between 0 and 1400 eV to determine the surface composition. The chemical state analysis was performed with a refined energy step of 0.1 eV in the C1s, U4f and O1s regions to define the peak positions accurately. The spectrum was aligned with the C1s signal, which was fixed to a position of 284.8 eV. This signal was present on all sample surfaces and stems from adventitious carbon. The fitting routine was performed with a 70% Gauss-Lorentz peak shape [80] with a Shirley background [81]. In order to define a pure U(IV) signal on the surface, a slightly oxidized $UO_2$ pellet was sputtered for 1 minute with an $Ar^+$ beam (E=0.110 kV) to expose a stoichiometric $UO_2$ surface. The FWHM of the pure component could then be defined as well as the Gauss-Lorentz distribution of the peak shape. Literature values of the $U4f_{5/2}$- and $U4f_{7/2}$-peak and satellite positions can be found in the works of Ilton and Bagus [67], Maslakov et. al. [82], Santos et. al. [49], and Van den Berghe et. al. [83]. A summary of these values is shown in Table 3.

*Table 3 – Characteristic features of the U(IV), U(V), U(VI) states and associated $U4f_{5/2}$-satellite positions.*

| Uranium oxidation State | Position (eV) [67, 82] | FWHM (eV) [49] | $U4f_{5/2}$-satellite shift (eV) [49] | $U4f_{5/2}$-satellite shift (eV) [83] |
|---|---|---|---|---|
| U(IV) | 380.0±0.2 | 1.65 | 7.0 | 6.7 |
| U(V) | 380.8±0.2 | 1.65 | 8.5 | 9.0 |
| U(VI) | 382.0±0.3 | 1.65 | 4.2, 10.0 | 4.0, 10.0 |

## 5.3. MOX experiment

The MOX pellets were annealed in 5% $H_2$ in $N_2$ at 1200 °C for 5h (with a 1h heating and cooling period, respectively) prior to the experiments in a 1000-2560-FP20 High Temperature graphite

furnace (Thermal Technology) inside a glove box with $N_2$ atmosphere. The pellets were then brought into the gas purged 150 or 250 mL 10 mM NaCl + 2 mM $NaHCO_3$ autoclave solutions contained in glass beakers in the autoclaves. The autoclave bolts were tightened in a vise using a torque wrench with 10 Nm moment, which significantly deformed the graphite gasket. Several aliquots of ~7.5 mL were taken throughout the experiment. These aliquots were ultra-centrifuged, after which the supernatant solution was taken for α-spectrometry and ICP-MS analysis.

## 5.4 Fe-Ca-$UO_2$-$CO_3$-system

The iron foils were placed at the bottom of 25 mL plastic vials that were then filled with 20 mL of the 10 mM NaCl + 2 mM $NaHCO_3$ or 9 mM NaCl + 1.5 mM $NaHCO_3$ + 0.5 mM $CaCO_3$ solutions. The foils were bent to maximize the contact between the foil and the solution. The entirety of the experiments were conducted in the Inert Technology glovebox, with oxygen partial pressure of $p_{O2} \leq 1$ ppm. Brief spikes in $O_2$ partial pressure occurred due to opening and closing of the entry chambers due to insufficient pumping of the chambers. The $O_2$ partial pressure was however quickly restored by the continuous flow through a purifier column with a catalytic bed.

# 6. Results and Discussion

## 6.1. Dose-rate modelling

### 6.1.1. MOX pellet dose-rates

The α-particle dose-rate of the 24 wt% MOX pellet with 4.96 GBq/g specific α-activity was modelled as a function of water depth perpendicular to the pellet surface, as described in Paper II [36]. The radiolytic production of $H_2O_2$ was calculated using $G(H_2O_2)$=0.985 molecules/100 eV [27]. The α-dose-rate profile can be seen in Figure 6, with radiolytic production shown on the y-axis on the right. As can be seen in Figure 6, the Bragg-peaks are averaged out over the water depth as a high number of particles are simulated. The ASTAR and SRIM with PRAL models correspond well with each other, with the SRIM with PRAL giving a slightly lower dose-rate over the entire α-particle range in water. The 5.44 MeV average α-particle energy had a projected range of 13.5 µm using SRIM with PRAL in the MOX matrix, compared to 14.1 µm using ASTAR with CSDA. Using the ASTAR data, the average dose-rate over the α-particle range in water, corresponding to 43.5 µm, is equal to 8.699 kGy/h. This corresponds to a $H_2O_2$ production rate of $1.49 \cdot 10^{-7}$ mol/d, or equivalently in a 200 mL solution a $H_2O_2$ production of $7.43 \cdot 10^{-7}$ mol/L·d. Using the SRIM with PRAL data, the α-particle range in water is 41.7 µm, giving an average dose-rate of 8.853 kGy/h.

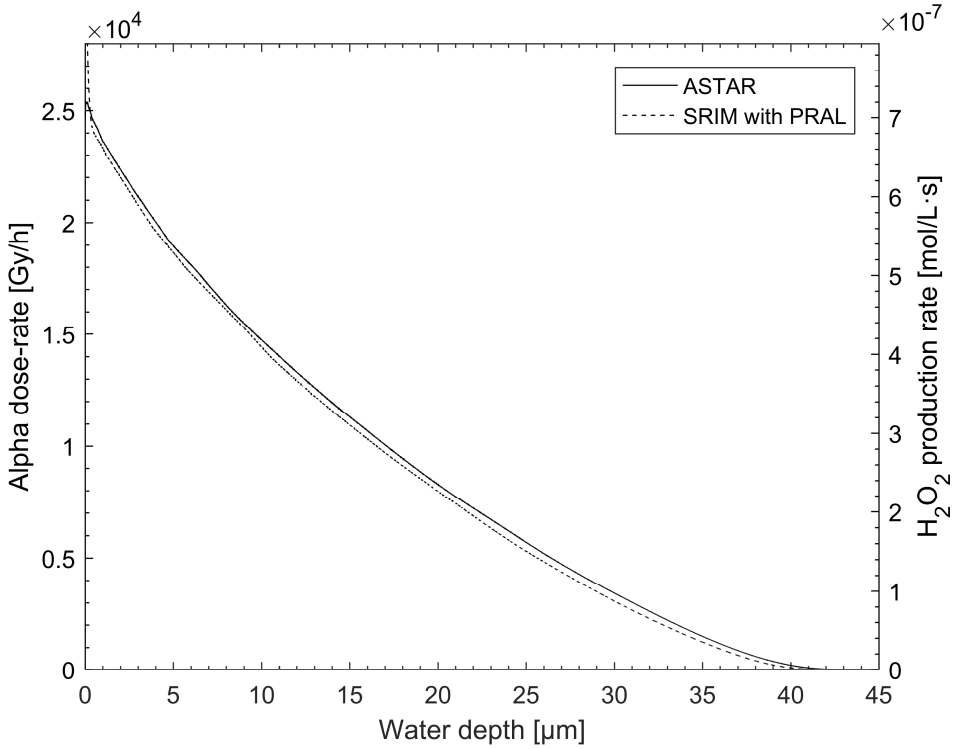


*Figure 6 – Dose-rate and production rate of $H_2O_2$ from a 24 wt% doped MOX-pellet as a function of water depth using ASTAR and PRAL corrected SRIM models.*

Using the ASTAR model to calculate the $H_2O_2$ production rate of the 10% pellet pieces yields $4.40 \cdot 10^{-8}$ mol/d and $4.17 \cdot 10^{-8}$ mol/d for the slightly bigger and smaller MOX slices (Table 2).

### 6.1.2. Am-241 dose-rate

The α-dose-rate and $H_2O_2$ production in the 30 µm layer between the 3.30 MBq Am-241 source and the $UO_2$ pellet was modelled. As there is a lack of stopping power data for $AmO_2$, it was estimated as $UO_2$ with a 95% density. The Am-241 sources are covered by a 2 µm gold layer, and ASTAR mass stopping powers for gold are used to account for the attenuation in this layer. Using the ASTAR database combined with the CSDA approach, the dose-rate profile was calculated and is shown in Figure 7. The gold layer had quite a high influence on the energy of the α-particles, and few α-particles had a range longer than 30 µm in water. Therefore, few α-particles from the Am-241 source reach the $UO_2$ surface. The Pyrex glass threads were not considered in the calculation as they cover a small fraction of the total surface area and were assumed to absorb less than 1% of the total dose.

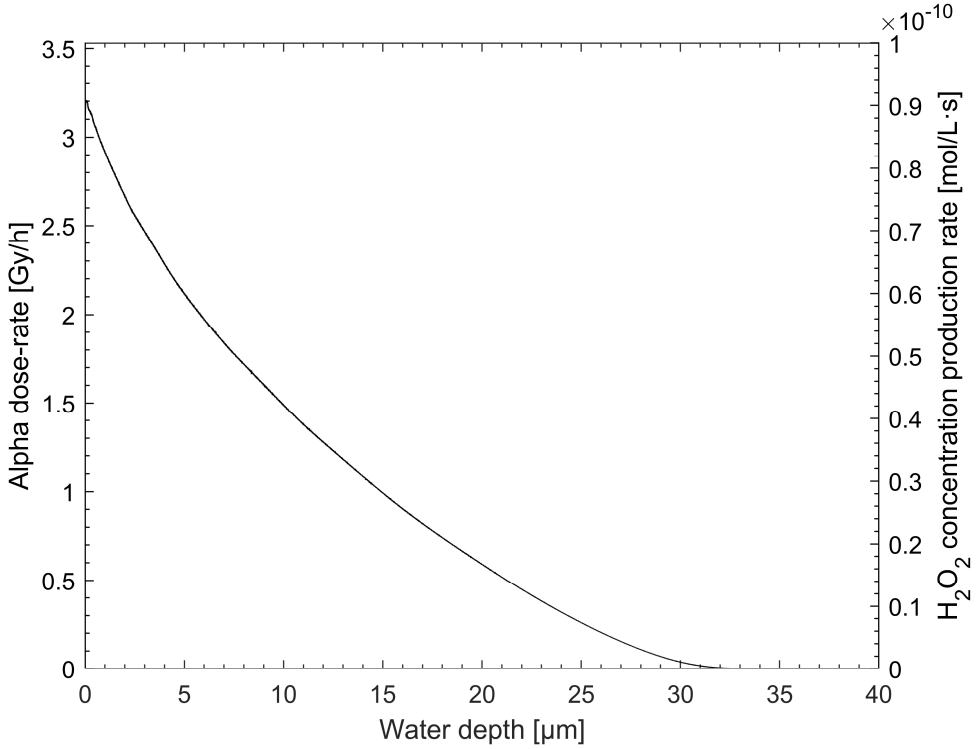


*Figure 7 – Modelled α-dose-rate from the 3.30 MBq Am-241 source as a function of water depth perpendicular to the surface of the source.*

The 30 µm water layer between the 3.30 MBq Am-241 source and $UO_2$ surface corresponds to an irradiated volume $V_{irr}$ = (11.5 mm/2)$^2$·π·0.03 mm = 3.12 mm$^3$. For the 11-days experiments, the total $H_2O_2$ production in $V_{irr}$ is 3.12·10$^{-5}$ M. This equivalently corresponds to 1.28·10$^{-4}$ M over the 45-day period. This is sufficient to cause locally acidic conditions if a significant fraction of the produced $H_2O_2$ reacts with the $UO_2$ surface through the anodic dissolution reaction (Eq 10). This effect is diminished by the buffer capacity of $HCO_3^-$. However, the locally acidic conditions will be strongly dependent on the convection into the bulk solution. As there is no stirring, the advection is zero and the solution mixing will be purely diffusion-controlled.

## 6.2. Dissolution experiments

### 6.2.1. NaHCO3 solution experiments

Two $UO_2$ pellets were separated at a 30 µm distance from the 3.30 MBq Am-241 source in 10 mM $NaHCO_3$ solution under 10 bar Ar and $H_2$ atmospheres, respectively. Samples of ~7.5 mL were measured using ICP-MS. The measured uranium concentrations in solution throughout the experiment are shown in Figure 8, together with the solubility of U(IV)(am) from the work of Neck and Kim [25]. During the first 15-day period, the uranium concentrations were stagnant before increasing quite rapidly under Ar atmosphere. The samples from the Ar atmosphere series were ultracentrifuged and showed no evidence of colloids. After 13 days, the concentration under $H_2$ atmosphere was unexpectedly somewhat higher than under Ar atmosphere over the same time period but was lower in all subsequent data points. The very slow increase in uranium concentration under $H_2$ atmosphere indicates that $H_2$ has an inhibiting effect on the oxidative dissolution of $UO_2$. The $NaHCO_3$ solution volumes, duration of the experiments and dissolved uranium concentrations can be seen in Table 4, together with the data from the MQ experiments.

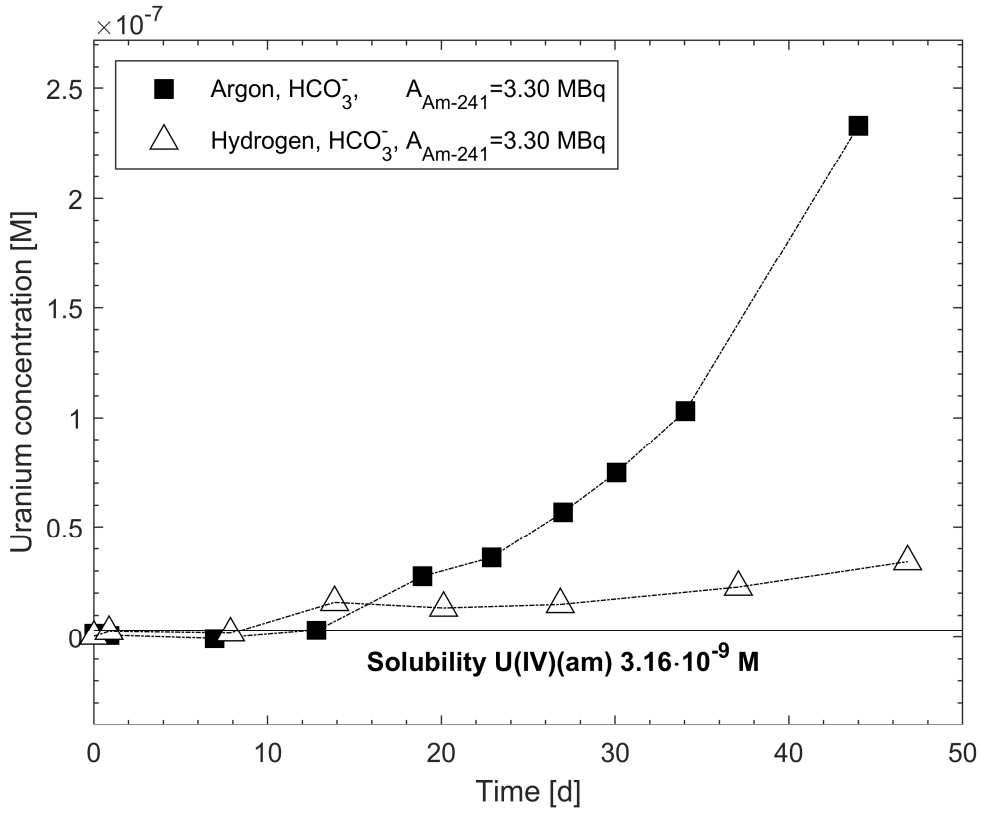


*Figure 8 – Dissolved uranium concentrations in the 10 mM $NaHCO_3$ solution in contact with the $UO_2$ pellet exposed to the 3.30 MBq Am-241 source under Ar and $H_2$ atmospheres. The solubility of U(IV)(am) shown is obtained from the work of Neck and Kim [25].*

### 6.2.2. MQ water experiments

$UO_2$ pellets were exposed to the 1.85 MBq Am-241 source in MQ water under both 10 bar Ar and $H_2$ atmospheres for 11 days. Under $H_2$ atmosphere the dissolved uranium concentrations were below the detection limit of the ICP-MS measurement. The same was seen in one of the two 11-day 1.85 MBq experiments under Ar atmosphere, where the concentration in the first experiment (Ar, 10 bar 1) was below the detection limit, while in the second experiment (Ar, 10 bar 2) the concentration reached $5.1 \cdot 10^{-8}$ M (Table 4). Using the 3.30 MBq Am-241 source for 11 days in MQ water yielded higher concentrations. Both of the 11-day exposures using the 3.30 MBq source under Ar atmosphere gave higher concentrations at the end of the experiments as compared to approximately the same time period in $NaHCO_3$ solution. This is somewhat unexpected, since $HCO_3^-$ complexes U(VI) efficiently, forming a soluble complex [84]. However, the significantly different solution volumes might influence the dissolution.

By dissolving U(VI), there is no oxidation product on the surface blocking further oxidation [29]. In addition, the inclusion of $HCO_3^-$ would buffer the pH at 8.34, which could influence the dissolution kinetics. The same behaviour was observed in the work of de Pablo et. al., where the dissolution rate of $UO_2$ was initially slower in the presence of $HCO_3^-$ as compared to in MQ water [85]. This was suggested to be due to radical scavenging by the $HCO_3^-$ ion. The scavenging of the radical radiolysis products could result in a lower net production of $H_2O_2$ and therefore a lower oxidation of the $UO_2$ surface. However, $HCO_3\cdot$ is also a strong oxidant, making the scavenging effect somewhat hard to assess.

The 3.30 MBq $NaHCO_3$ solution experiment in Ar atmosphere gave a factor of two higher dissolved uranium concentration as compared to the corresponding MQ experiment after 45 days. This was also observed in the work of de Pablo et. al., where the final concentration under $HCO_3^-$ solution was higher as compared in in MQ water [85]. In the 11-days and 45-day exposure to the 3.30 MBq source in MQ water experiments under Ar atmosphere, the solution volumes were different. Therefore, the total dissolved uranium was roughly a factor of two higher in the longer experiment, despite the lower concentration. A sample was taken out of the glove box at the end of the 45-day MQ experiment and was measured using a pH electrode under air atmosphere. The measured pH was 6.9±0.5, which might have been affected by the air exposure. The ionic strength in this sample is also very low, which makes the uncertainty of the measurement high. The pellets from the MQ experiments were measured using XPS at the end of the experiment.

In the study performed by Sunder et. al. [50], using Am-241 sources with activities up to 14.8 MBq, the exposure times to the Am-241 sources were considerably shorter (100 h) and were also performed at 100 °C, making their data hard to compare to the results in this work. The uranium concentration measurements using the Bromo-PADAP method in the work of the researchers also had a very high uncertainty. Despite this, some trends could be discerned. Under $H_2$ atmosphere, Sunder et. al. found that the uranium concentrations were seemingly decreasing with increasing Am-241 source strength. Under $N_2$ atmosphere, the opposite was true, with an increasing dissolved uranium concentration with increasing source strength. The concentrations were generally in the

order $10^{-8}$ M. There was no significant difference in the dissolved concentrations between $H_2$ and $N_2$ atmospheres in the work of the researchers. This is different to the results in this work, where the $H_2$ atmosphere significantly reduced the dissolved concentrations of uranium by approximately a factor of 10 (Table 4). Generally, under Ar atmosphere the concentrations were in the order of $10^{-7}$ M, as compared to $10^{-8}$ M under $H_2$ atmosphere. This trend was seen in both the MQ and $NaHCO_3$ solution experiments.

*Table 4 - Concentrations, volumes and times of all the external irradiation experiments.*

| $A_{Am-241}$ [MBq] | Atmosphere | Volume [mL] | $NaHCO_3$ [M] | Time [d] | Uranium concentration [M] |
|---|---|---|---|---|---|
| 1.85 | $H_2$, 10 bar 1 | 45.09 | 0 | 11 | - † |
| 1.85 | $H_2$, 10 bar 2 | 44.06 | 0 | 11 | - † |
| 1.85 | Ar, 10 bar 1 | 45.15 | 0 | 11 | - † |
| 1.85 | Ar, 10 bar 2 | 42.73 | 0 | 11 | $5.09 \cdot 10^{-8}$ |
| 3.30 | $H_2$, 10 bar 1 | 44.43 | 0 | 11 | $1.84 \cdot 10^{-8}$ |
| 3.30 | $H_2$, 10 bar 2 | 43.34 | 0 | 11 | $3.53 \cdot 10^{-8}$ |
| 3.30 | Ar, 10 bar 1 | 43.45 | 0 | 11 | $2.29 \cdot 10^{-7}$ |
| 3.30 | Ar. 10 bar 2 | 43.64 | 0 | 11 | $3.19 \cdot 10^{-7}$ |
| 3.30 | Ar, 10 bar | 153.01 | 0 | 45 | $1.26 \cdot 10^{-7}$ |
| 3.30 | $H_2$, 10 bar | 154.54 | $10 \cdot 10^{-3}$ | 47 | $3.42 \cdot 10^{-8}$ |
| 3.30 | Ar, 10 bar | 153.93 | $10 \cdot 10^{-3}$ | 44 | $2.33 \cdot 10^{-7}$ |

† Below the detection limit of the ICP-MS measurement.

## 6.3. XPS study of irradiated $UO_2$

### 6.3.1. Characteristics of the U(IV) 4f7/2-peak

The slightly oxidized $UO_2$ pellet surface was sputtered for 1 minute (0.110 kV $Ar^+$-beam) to remove the oxidized surface layer. The U4f spectrum of the sputtered surface is shown in Figure 9. The $U4f_{5/2}$- and $U4f_{7/2}$-peak positions are significantly lower than literature values, by approximately 0.5 eV [67, 82]. The separation between the $U4f_{5/2}$- and $U4f_{7/2}$-peak positions is however maintained, which indicates that the whole spectrum is shifted by ~0.5 eV. This can be due to charging correction procedures, as noted in the work of Van den Berghe et. al., where a 0.5 eV systematic shift was found in their measurements of cesium uranates [83]. In the measurement of the sputtered pellet, distinct $U4f_{5/2}$- and $U4f_{7/2}$-satellites with $\Delta$=6.9 eV separation from their main peaks indicate a pure U(IV) oxidation state on the surface.

The pure U(IV) signal on the sputtered surface can be seen in the $U4f_{7/2}$-envelope in Figure 10. The peak could be fitted with a 70% Gauss-Lorentz, 1.7 eV FWHM peak at a binding energy of 379.5 eV. The same parameters and systematic shift have been used in the fitting procedure of the peak deconvolution process throughout this work.

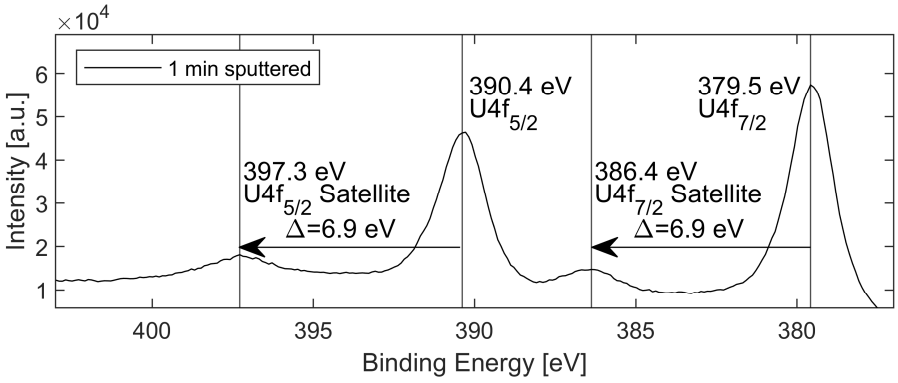


*Figure 9 – The U4f spectrum of the 1-minute sputtered (0.110 kV $Ar^+$-beam) $UO_2$ pellet, giving low binding energy positions of the $U4f_{7/2}$ and $U4f_{5/2}$ peaks.*

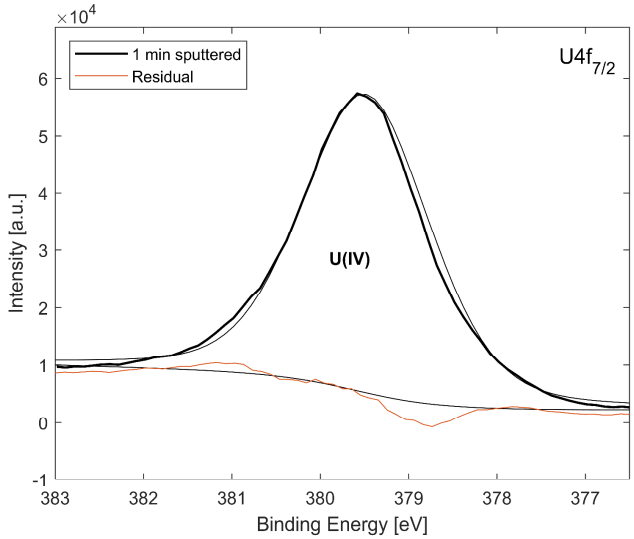


*Figure 10 – Deconvolution of the $U4f_{7/2}$ peak in the U4f spectra of the sputtered $UO_2$ pellet. A pure U(IV) signal is found in the peak deconvolution, with FWHM=1.7 eV and 70% Gauss-Lorentz peak shape.*

### 6.3.2 Initial surface reference states

Two pellets were measured using XPS after their initial washing process in 50, 10, 10 and 0 mM $NaHCO_3$ solutions. Their U4f spectra are shown in Figure 11. Despite the long washing process, the pellets have a higher surface oxidation state than the pure U(IV) signal based on the $U4f_{7/2}$-peak positions, which are 0.3 and 0.5 eV, respectively, higher than the reference state. This indicates a contribution to the peak position of the U(V) and U(VI) oxidation states in the $U4f_{7/2}$ envelope. De Pablo et. al. studied the oxidation state of $UO_2$ pellets after long 10 mM $HCO_3^-$ washes and found that the surface oxidation state was reduced to $UO_{2.05}$ after 100-days exposure [86]. This indicates a very slow process of dissolving oxidized uranium using a batch $HCO_3^-$ washing setup. The data from de Pablo et. al. shows that $HCO_3^-$ complexes uranium on oxidized surfaces below the oxidative dissolution threshold, i.e. it is able to reduce the surface well below $UO_{2.33}$ [86], which corresponds well with the results in this work.

Peak deconvolution of the $U4f_{7/2}$-peaks shown in Figure 11 of the washed $UO_2$-pellets was performed. The resulting deconvolutions and fitting of the two reference pellets can be seen in Figure 12a and Figure 12b. The deconvolution of the first reference pellet surface yields an area ratio of U(V)/U(IV)=0.47, which is equivalent to $UO_{2.16}$ ($(UO_2+0.47\cdot UO_{2.5})/1.47=UO_{2.16}$). Similarly, the second reference pellet has a ratio U(V)/U(IV)=0.56 and U(VI)/U(IV)=0.05, corresponding to $UO_{2.21}$. The transport vessel is equipped with an O-ring and is made to fit with the specific sample entry chamber of the XPS instrument. It is therefore unlikely that the pellet surfaces oxidize during the transport to the instrument. The washing times might be too short to reduce the pellet surfaces further, or the atmosphere in the glove box was too oxidizing with $p_{O2}\leq 1$ppm.

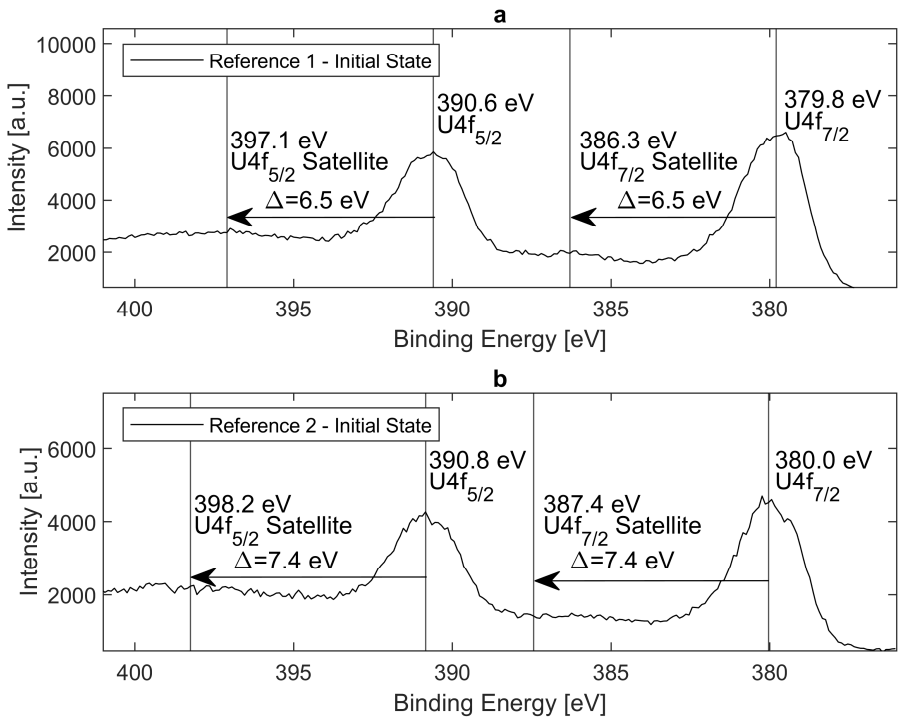


*Figure 11 – U4f-states of the carbonate washed $UO_2$ pellets showing the $U4f_{5/2}$, $U4f_{7/2}$-peaks and their corresponding satellite peaks.*

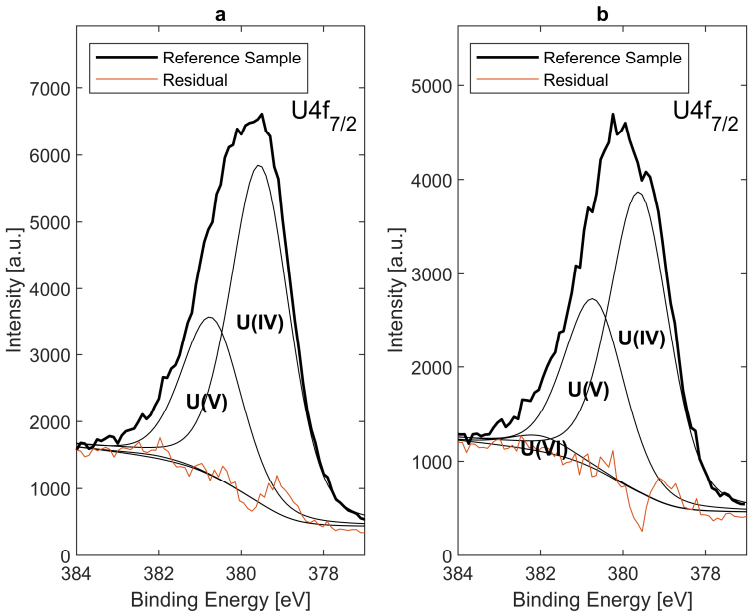


*Figure 12 – Deconvolution of the U4f$_{7/2}$ peaks on the carbonate washed UO$_2$ pellet surfaces into their U(IV), U(V) and U(VI) components, showing (a) UO$_{2.16}$ and (b) UO$_{2.21}$ states.*

### 6.3.3. 11-day exposure under Ar atmosphere – first experiment

The U4f-spectra after the first 11-day exposure experiments in MQ under Ar atmosphere using the 1.85 and 3.30 MBq Am-241 sources are shown in Figure 13a and Figure 13b, respectively. No initial measurement was performed on these pellets, so the initial state has to be estimated by other initial state measurements, such as the reference pellet measurement shown in Figure 11. The pellet exposed to the 1.85 MBq Am-241 source had a slightly lower U4f$_{7/2}$-peak position as compared to the reference cases shown in Figure 11. However, this shift might not be significant. The pellet exposed to the 3.30 MBq Am-241 source shows a significantly higher U4f$_{7/2}$-peak position as compared to the reference pellets, which indicates that the stronger Am-241 source is sufficiently strong to significantly oxidize the pellet surface.

The deconvolution of the U4f$_{7/2}$-peak in the spectra of the UO$_2$ pellet exposed to the 1.85 MBq source gave U(V)/U(IV)=0.26 and U(VI)/U(IV)=0.02, as shown in Figure 14a. This corresponds to UO$_{2.11}$. The 1.85 MBq source therefore seems to oxidize the surface at a rate that is slower than the dissolution rate of U(V) and potentially U(VI) into solution, as the oxidation state would represent a reduction as compared to the reference pellets. This would indicate that the dissolution is sufficiently fast to prevent any oxidized layer from building up on the surface under exposure to the 1.85 MBq source. Alternatively, the initial state of the UO$_2$ surface was lower than in the reference cases, as there is some variance in the sample preparation procedure. This is supported by the low dissolved uranium concentration, as the ICP-MS measurement gave a signal below the detection limit. Deconvoluting the U4f$_{7/2}$-peak of the pellet exposed to the 3.30 MBq source gives U(V)/U(IV)=6.34, and U(VI)/U(IV)=1.36, corresponding to UO$_{2.52}$. This is a significantly oxidized surface oxidation state as compared to the reference state.

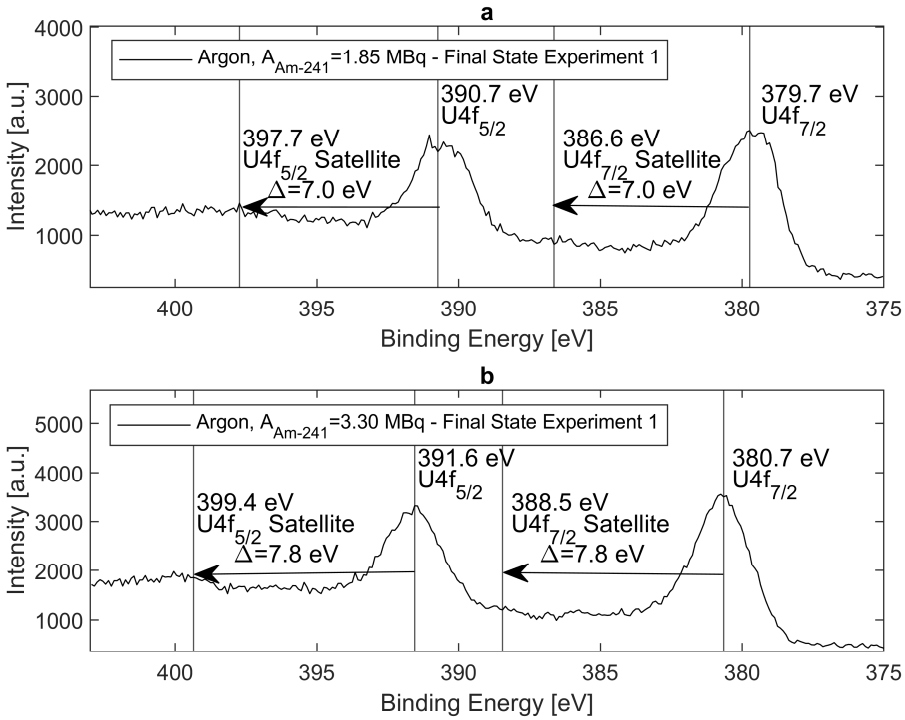


*Figure 13 – The U4f-spectra of the $UO_2$ pellets exposed for 11 days to the (a) 1.85 MBq and (b) 3.30 MBq Am-241 sources in MQ water under Ar atmosphere. First experiment.*

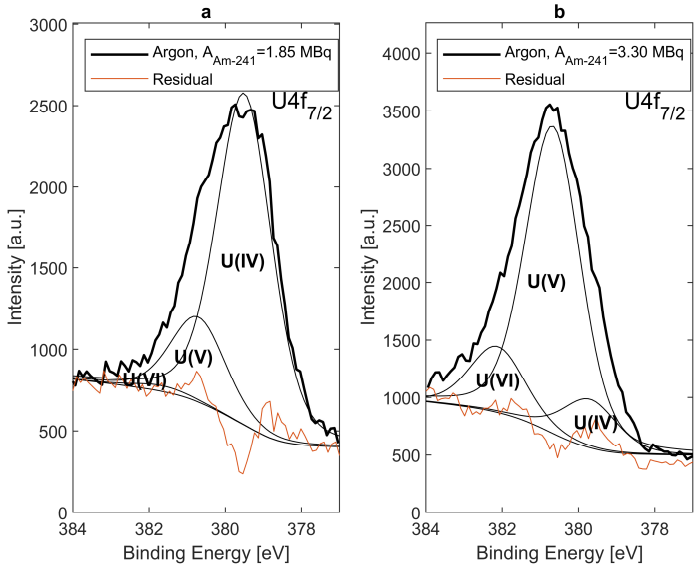


*Figure 14 – Deconvolution of the U4f$_{7/2}$ peaks of the U4f-spectra of the $UO_2$ pellets exposed for 11 days to the (a) 1.85 MBq and (b) 3.30 MBq Am-241 sources in MQ water under Ar atmosphere, showing the (a) $UO_{2.11}$ and (b) $UO_{2.52}$ states. First experiment.*

### 6.3.4. 11-day exposure under Ar atmosphere – second experiment

The 11-day exposure experiment in MQ water under Ar atmosphere was repeated with an XPS measurement of the initial oxidation state directly after the washing procedure. The pellets were exposed to the 1.85 and 3.30 MBq Am-241 sources for 11 days and were subsequently measured again using XPS. The initial U4f-spectra after the washing process of the $UO_2$-pellets prior to exposure is shown in Figure 15. The $U4f_{7/2}$-peak position seen in Figure 15a is higher than the reference pellet cases, indicating that the washing procedure was not as efficient as in the previous cases. The $U4f_{7/2}$-peak position in Figure 15b however corresponds very well with the reference pellet measurements.

After exposure to the Am-241 sources for 11 days in MQ water under Ar atmosphere, the surface oxidation states were measured. The U4f-spectra are shown in Figure 16. Both of the final U4f states correspond very well with the final states after the first Ar atmosphere experiment, showing a consistent final state after exposure to the sources. The pellet that was exposed to the 1.85 MBq Am-241 source shows a significantly lower $U4f_{7/2}$-peak position as compared to the initial state. The shift amounts to 0.6 eV, indicating that the 1.85 MBq source oxidizes the $UO_2$ surface at a significantly slower rate than the oxidized layer can dissolve in MQ water, which was also noted in the first experiment under Ar atmosphere. The $U4f_{7/2}$-peak deconvolution yields $UO_{2.07}$, slightly lower than in the first experiment. The pellet exposed to the 3.30 MBq Am-241 source had a significant shift in the $U4f_{7/2}$-peak position of 0.8 eV. The peak deconvolution of the $U4f_{7/2}$-peak yields an equivalent oxidation state of $UO_{2.44}$.

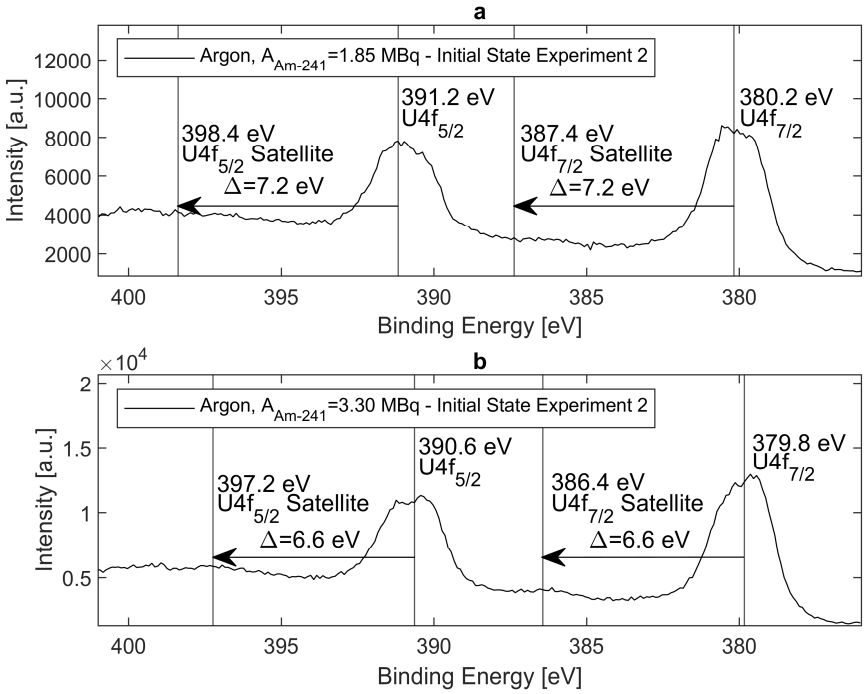


*Figure 15 – Initial U4f-spectra of the $UO_2$ pellets after their carbonate washing procedure and prior to exposure to the (a) 1.85 MBq and (b) 3.30 MBq Am-241 sources under Ar atmosphere.*

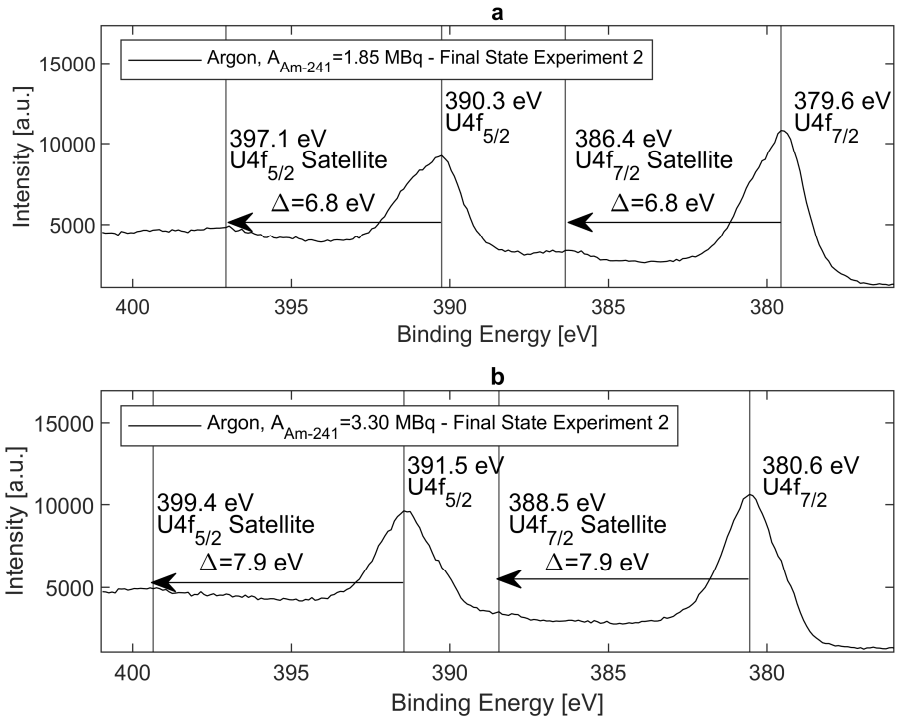


*Figure 16 – The U4f-spectra of the $UO_2$ pellets exposed for 11 days to the (a) 1.85 MBq and (b) 3.30 MBq Am-241 sources in MQ water under Ar atmosphere. Second experiment.*

### 6.3.5. 45-day exposure to the 3.30 MBq source under Ar atmosphere

The initial state of the $UO_2$ pellet before the 45-day exposure to the 3.30 MBq source in MQ water under Ar atmosphere was not measured, and the U4f spectrum has to be compared to the reference cases (Figure 11) and initial cases in the other experiments (Figure 15 and Figure 21). The exposure resulted in a significant shift of the U4f$_{7/2}$-peak position as compared to the reference samples. However, the shift is somewhat lower than the one observed in the 11-day experiment. It should be noted that the 45-day experiment was performed in ~154 mL solution, as compared to the ~45 mL in the 11-day experiment. This might lead to a somewhat higher dissolution rate under the 45-day exposure experimental setup.

The peak deconvolution of the U4f$_{7/2}$-peak envelope is shown in Figure 18. The deconvolution gives U(V)/U(IV)=1.88, equivalent to $UO_{2.33}$, which corresponds to the oxidative dissolution threshold [50]. $UO_{2.33}$ is a less oxidized state than the one found at the end of the 11-day experiment. However, the total dissolved uranium concentration at the end of the 45-day experiment is a factor of two higher.

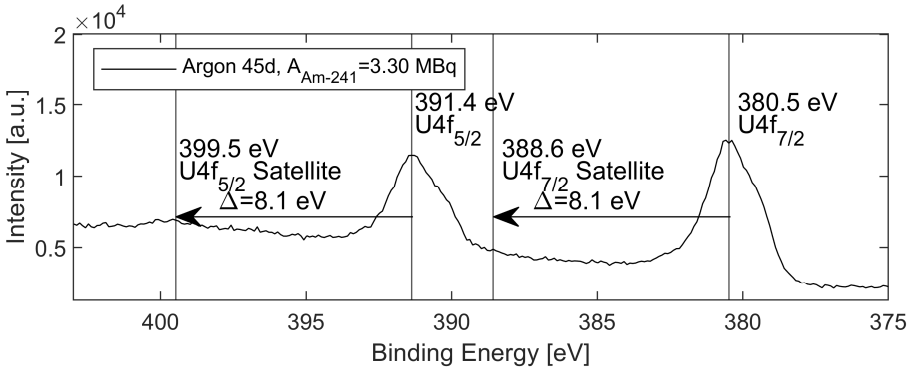


*Figure 17 – The U4f-spectrum of the $UO_2$-pellet exposed for 45 days to the 3.30 MBq Am-241 source in MQ water under Ar atmosphere.*

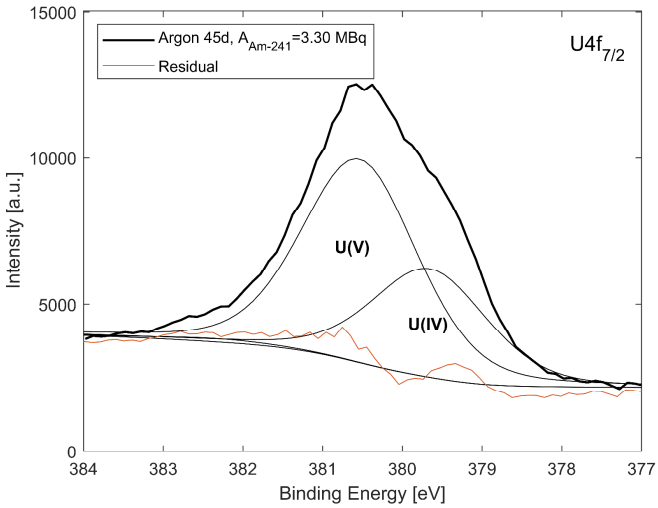


*Figure 18 – Deconvolution of the U4f$_{7/2}$ peak in the U4f spectrum of the $UO_2$ pellet exposed for 45 days to the 3.30 MBq Am-241 source under Ar atmosphere. The peak deconvolution showed the $UO_{2.33}$ state.*

### 6.3.6. 11-day exposure under H2 atmosphere – first experiment

Two pellets were exposed for 11 days to the 1.85 and 3.30 MBq Am-241 sources in MQ water under $H_2$ atmosphere. No initial surface oxidation state measurements were performed, and the analysis has to be made in relation to the reference cases in Figure 11, as well as initial oxidation states in the other experiments (Figure 15 and Figure 21). The $UO_2$ pellet that was exposed to the 1.85 MBq source gave a slightly lower U4f$_{7/2}$-peak position as compared to the reference pellet peak positions. This indicates a slightly reduced surface, as was also indicated in the Ar atmosphere experiments. The $UO_2$ pellet exposed to the 3.30 MBq source showed a significant positive shift in the U4f$_{7/2}$-peak position by approximately 0.5 eV as compared to the reference cases. However, this shift is somewhat lower than the shift observed in the Ar atmosphere experiments, where the resulting shift was 0.1-0.2 eV higher. This indicates that $H_2$ might have a protective effect towards radiolytic oxidation, but the difference might not be statistically significant.

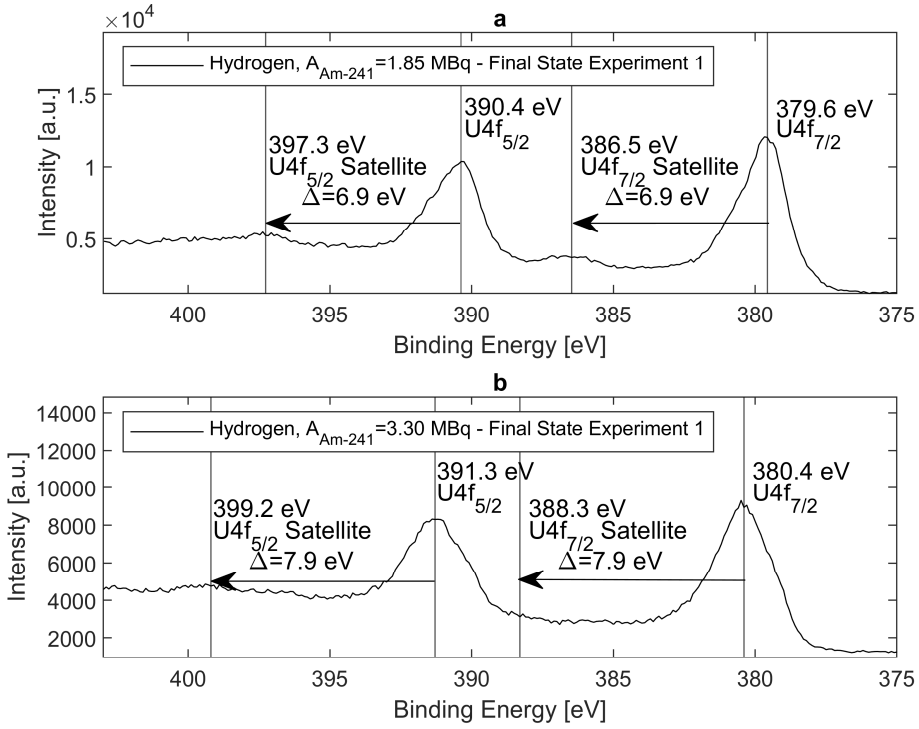


*Figure 19 – The U4f-spectra of the $UO_2$ pellets exposed for 11 days to the (a) 1.85 MBq and (b) 3.30 MBq Am-241 sources in MQ water under $H_2$ atmosphere. First experiment.*

The $U4f_{7/2}$-peaks from the $H_2$-atmosphere experiments were deconvoluted and the results can be seen in Figure 20a and Figure 20b. The $UO_2$ pellet exposed to the 1.85 MBq source shows a reduction both in the U4f spectrum and in the deconvolution, as U(V)/U(IV)=0.28 is equivalent to $UO_{2.11}$. The deconvolution of the pellet exposed to the 3.30 MBq source gave U(V)/U(IV)=2.56 and U(VI)/U(IV)=0.31, which corresponds to $UO_{2.41}$. This is unexpectedly somewhat higher than the oxidation state of the pellet exposed to the source for 45 days under Ar atmosphere. However, the surface is still slightly less oxidized than after the two 11-day exposure experiments under 10 bar Ar atmosphere of $UO_{2.52}$ and $UO_{2.44}$. The U(VI) component in the peak deconvolution process, as seen in Figure 20b, matches the large residual of the deconvolution very well and might therefore be an error in the fitting procedure. Repeating this experiment with initial and final surface oxidation state measurements allows for investigating this source of error.

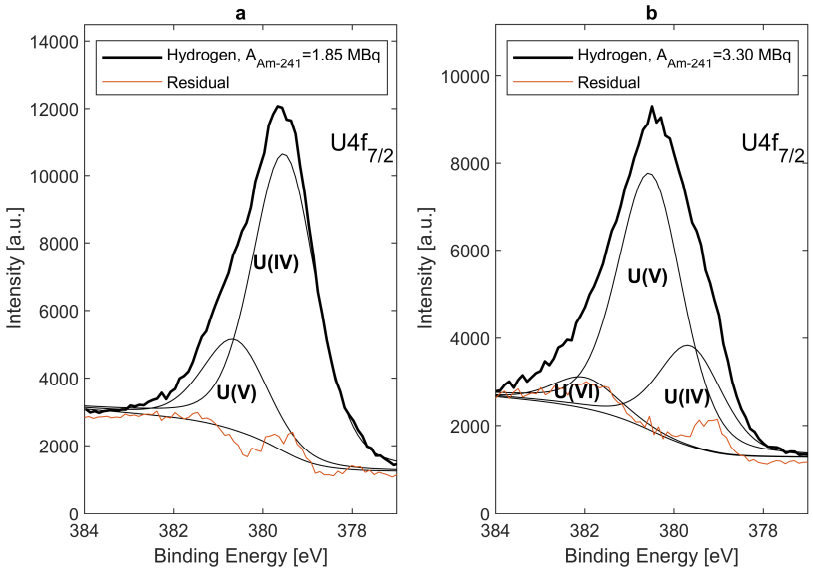


*Figure 20 – Deconvolution of the U4f$_{7/2}$ peaks of the U4f-spectra of the UO$_2$ pellets exposed for 11 days to the (a) 1.85 MBq and (b) 3.30 MBq Am-241 sources in MQ water under H$_2$ atmosphere, showing the (a) UO$_{2.11}$ and (b) UO$_{2.41}$ states. First experiment.*

### 6.3.7. 11-day exposure under H2 atmosphere – second experiment

The 11-day exposure experiment in MQ water under $H_2$ atmosphere was repeated with an XPS measurement prior to exposure, as previously described in the second Ar atmosphere experiment. The pellets were measured after the 11-day exposure period to the 1.85 and 3.30 MBq Am-241 sources. The initial U4f spectra of the two pellets after the washing procedure are shown in Figure 21a and Figure 21b. Both initial U4f spectra have a lower oxidation state as compared to the previous reference states and are close to stoichiometric $UO_2$ when looking at the U4f$_{7/2}$ and U4f$_{5/2}$ peak positions, as well as the satellites with a shift of $\Delta$=6.8 and 6.7 eV, respectively.

The U4f spectra after exposure to the 1.85 MBq and 3.30 MBq Am-241 sources can be seen in Figure 22a and Figure 22b, respectively. The spectra both remain practically unchanged as compared to the initial state, where the $UO_2$ pellet exposed to the 1.85 MBq source shows signs of a slight reduction in the U4f$_{7/2}$-peak position. The final U4f$_{7/2}$-peak position is slightly below the pure U(IV) peak position but is likely within the statistical margin of error. Deconvolution of the U4f$_{7/2}$-peak into its U(IV) and U(V) components yields U(V)/(U(IV)=0.03, equivalent to UO$_{2.02}$. The pellet exposed to the 3.30 MBq Am-241 source also showed no signs of oxidation as compared to the initial surface oxidation state. The deconvolution yields a somewhat larger U(V) component as compared to the 1.85 MBq exposed pellet and U(V)/U(IV)=0.08, equivalent to UO$_{2.04}$. The second experiment of the 11-day exposure to the 3.30 MBq source under $H_2$ atmosphere gave a different result compared to the first experiment, as can be seen by comparing the U4f$_{7/2}$-peak positions in Figure 19 and Figure 22, with a relative difference of 0.7 eV. However, the initial oxidation states on the sample surfaces showed quite a large degree of inconsistency. This makes the first experimental result under $H_2$ atmosphere somewhat uncertain, as it is possible that the

initial state was higher than in the second experiment. This makes the results from the second experiment more reliable, as the relative shift after the exposure time can be directly determined.

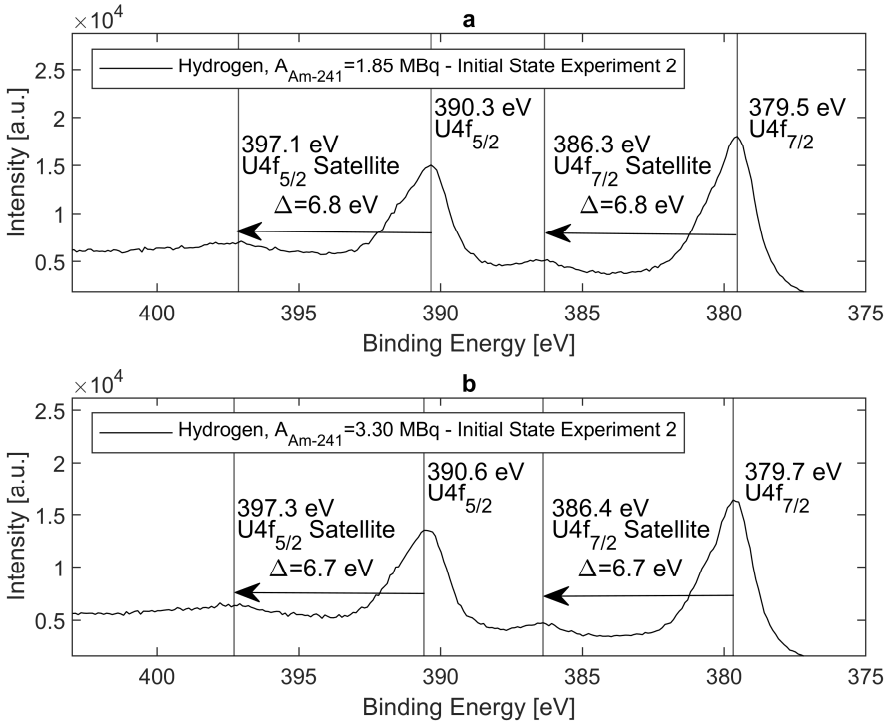


*Figure 21 – Initial U4f-spectra of the $UO_2$ pellets after their carbonate washing procedure and prior to exposure to the (a) 1.85 MBq and (b) 3.30 MBq Am-241 sources under $H_2$ atmosphere. Second experiment.*

The results in the second experiment under $H_2$ atmosphere are in agreement with previous studies of $UO_2$ oxidation in the presence of hydrogen. In a study by Carbol et. al. where a 10 wt% U-233 doped $UO_2$ pellet was studied under a $H_2$ atmosphere, uranium concentrations in the order of $9 \cdot 10^{-12}$ M were found [42]. This indicates a very low extent of oxidation of the $UO_2$ pellet under $H_2$ atmosphere under a substantially higher radiolytic production.

In all of the 1.85 MBq Am-241 source experiments the results showed a decrease in oxidation state as compared to initial or reference cases. This indicates a faster dissolution rate of the oxidized U(V) and U(VI) from the surface as compared to the radiolytic oxidation rate due to the Am-241 source. It is not likely that reduction of the uranium oxidation state occurred on the $UO_2$ surface due to radiolytic production. The amounts released into solution in the experiments using the weak source were below or close to the detection limit of the ICP-MS measurement, with only one Ar atmosphere experiment giving a measurable concentration of $5.1 \cdot 10^{-8}$ M. This is significantly lower than the concentrations found after exposure to the 3.30 MBq source under Ar atmosphere.

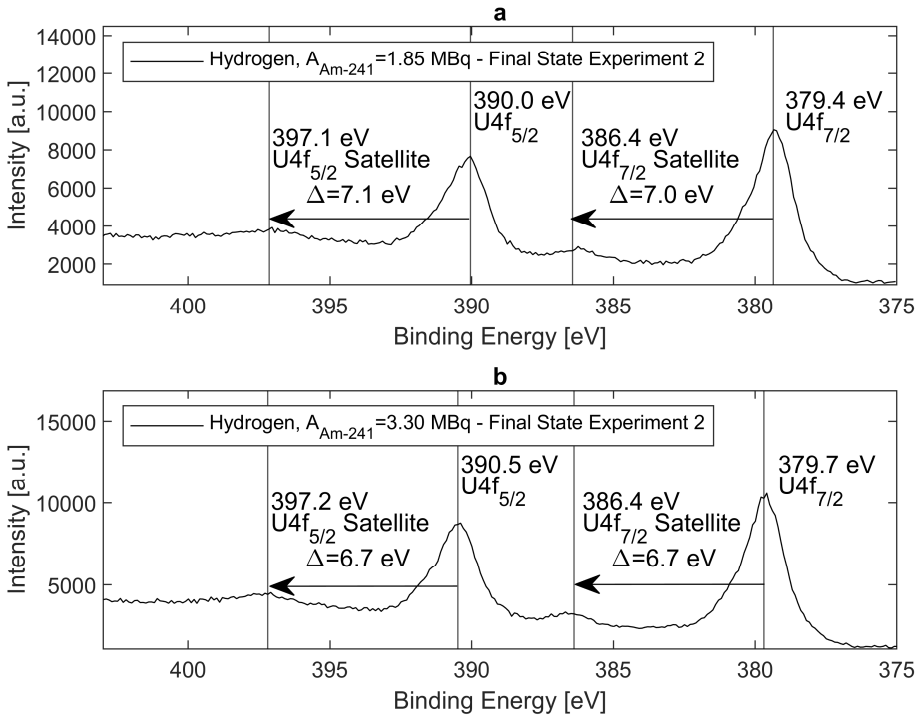


*Figure 22 – The U4f-spectra of the $UO_2$ pellets exposed for 11 days to the (a) 1.85 MBq and (b) 3.30 MBq Am-241 sources in MQ water under $H_2$ atmosphere. Second experiment.*

External α-radiolysis of $UO_2$ using α-sources has been studied by Sunder et. al. The researchers used Am-241 sources in triply distilled $N_2$-purged solutions at 100 °C [87]. The experimental setup was replicated to a large degree in this work, as they used α-sources that irradiated a 30 µm water layer in between the source and $UO_2$ surface, achieved by the use of Pyrex glass fibers. The exposure periods of 100 h were shorter than the ones studied in this work (~264 h). The surface oxidation state in the work of the researchers was measured through the deconvolution of the U4f$_{7/2}$-peak from the U4f XPS-spectra into its U(IV) and U(VI) components. In early XPS-studies, such as the work of Sunder et. al. [50], Delobel et. al. [88], as well as McIntyre et. al. [89], no U(V) component was included in the U4f$_{7/2}$-peak deconvolution process, as there was previously neither pure U(V) reference compounds nor studies that conclusively proved that U(V) was a component in an oxidized $UO_2$-surface layer [49].

The positions of the U(IV), U(V) and U(VI) components in the U4f$_{7/2}$-peak envelope have been reported by a number of authors as ~380, ~381 and ~382, eV respectively [14, 67-69]. Therefore, the 1.3 eV separation between the U(IV) and U(VI) components used by Sunder et. al. in their peak deconvolution instead of ~2 eV might not be accurate. This changes the result of the deconvolution process, as the U(IV) signal was set to a value between the now relatively established energies of the U(V) and U(VI) components. Sunder et. al. found that hydrogen suppresses the oxidation of the $UO_2$ surface. Since the temperature of 100 °C could thermally activate $H_2$ it was not evident if the activation on the $UO_2$ surface was involved with the suppression. The results from this work

indicate that $H_2$ activation on the $UO_2$ surface might be a significant mechanism in the suppression of oxidation of a $UO_2$ surface.

## 6.4. Dissolution experiments of MOX pellets

### 6.4.1. XRD of MOX pellets

The 10% MOX piece was analyzed using XRD after annealing in 5% $H_2$ in $N_2$ for 5 h at 1200 °C with a 1 h heating and cooling time. The majority of the peaks correspond to $(U_{0.85}Pu_{0.15})O_2$ as seen in Figure 23. However, the Pu content in $(U_{1-x}Pu_x)O_2$ is hard to discern with high precision using XRD without proper calibration standards and procedures, and the peaks likely correspond to that of $(U_{0.9}Pu_{0.1})O_2$. The fcc structure corresponding to the majority of the peaks has a lattice parameter of 5.4592 Å, which is consistent with $(U_{0.9}Pu_{0.1})O_2$, as the lattice parameter is 99.92% of the theoretical one of 5.4635 Å from Vergard's Law. However, there are secondary peaks at 29.1, 33.7, 48.4 and 57.4 degrees 2θ, which seem to correspond to a secondary fcc-phase that has a lattice parameter of 5.322 Å at hkl indexes 111, 200, 220, 311. This matches a UN or $UN_2$ phase. The phase corresponding to this lattice parameter was stable under the radiolytic oxidation experiments, as well as under additions of $H_2O_2$, which is uncharacteristic of UN and $UN_2$ phases. This might indicate that the nitride phase was retained in the bulk matrix, or that the phase is incorrectly identified. However, the phase was efficiently removed by annealing with 5% $H_2$ in Ar for 5 hours at 1200 °C, indicative of the nitride phase being removed. All the oxidative dissolution MOX experiments presented in this work were performed with the possible nitride phase present, which might affect the dissolution properties.

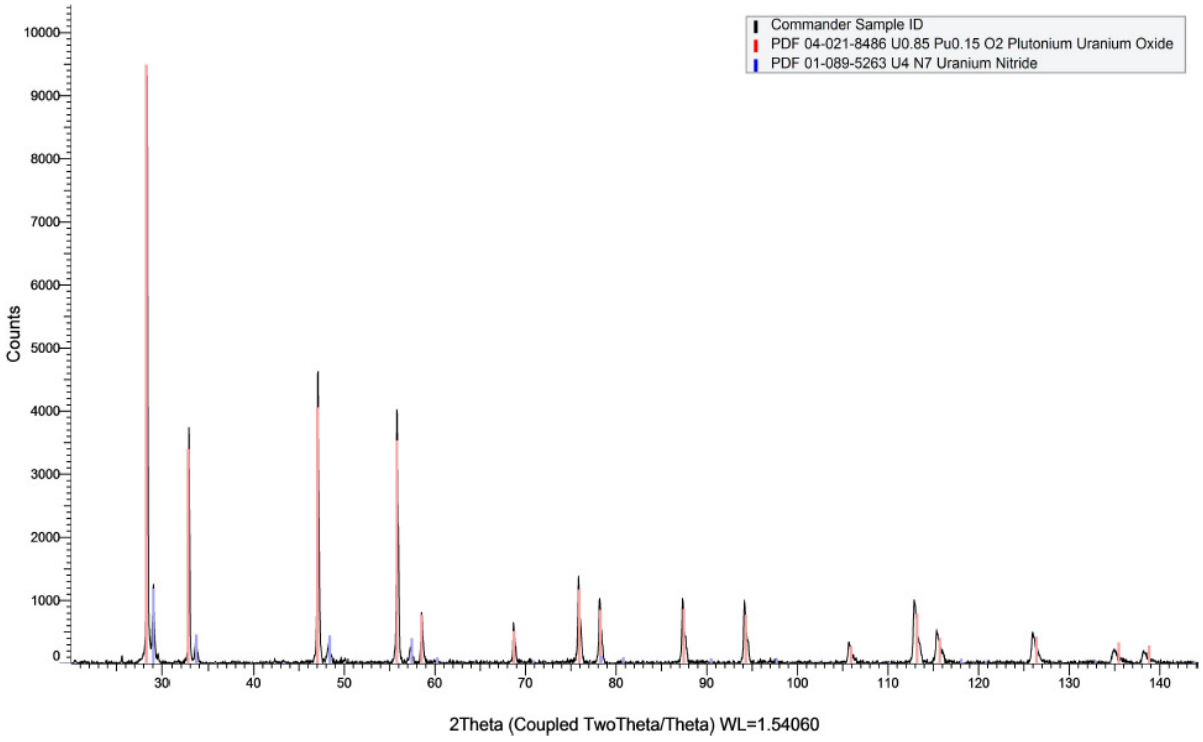


*Figure 23 - XRD pattern of the 10% MOX pellet showing $(U_{0.85}Pu_{0.15})O_2$ as well as UN peaks.*

### 6.4.2. Autoclave leakage

Inadequate pressure on the graphite gasket can significantly influence the experiment due to air leaking in. In previous work by our group, the sensitivity of the autoclave atmospheres to air contamination has been noted. Several experiments were conducted where the torque applied to the autoclave bolts was seemingly insufficient, leading to very high dissolution rates. This especially occurred in the $H_2$ atmosphere experiments, likely due to counter diffusion of air as $H_2$ leaks out through a slit. (If the leakage occurs through a circular hole, the counter diffusion rate is negligible, see appendix in [90]). Even under small gas leaks, the leaking in of air is significantly large to cause a rapid increase in dissolution rate. In-leakages of $O_2$ during sampling can potentially influence the autoclave atmosphere as well.

### 6.4.3. Ar atmosphere

The 10 and 24 wt% Pu-doped pellets were studied in 10 mM NaCl + 2 mM $NaHCO_3$ solution under 10 bar Ar atmospheres. The dissolved uranium concentration data is shown as a function of time in Figure 24. The two experiments using the 10% Pu-doped pellets show somewhat of a discrepancy. During the early stages of the experiment the dissolution rate of the MOX 10% Experiment 2 is significantly higher than in the MOX 24% Experiment 2, despite the lower degree of radiolytic production. After this initial period, the dissolution rate in the MOX 24% Experiment 2 became significantly higher than the 10% experiments, as would be expected from the composition. The dissolution rates indicate quite a high uncertainty in the experimental setup, especially during the early stages (~40 d).

A 10 bar Ar atmosphere experiment using the 24 wt% Pu-doped MOX has previously been conducted by Bauhn et. al., and is shown together with the data in Figure 24 [70] (Paper III). As can be seen from Figure 24, the dissolution rate in MOX 24% Bauhn et. al. is significantly higher during the first 50 days as compared to the MOX 24% Experiment 2. However, after 50 days, the dissolution rates reach roughly the same value. The slope of the last two data points in the previous MOX 24% experiment is $2.37 \cdot 10^{-6}$ M·d$^{-1}$. In the MOX 24% Experiment 2 the dissolution rate in the last data points reaches $1.94 \cdot 10^{-6}$ M·d$^{-1}$. These values can be compared to the $H_2O_2$ production rate using the ASTAR model equal to $1.49 \cdot 10^{-7}$ mol/d. As the remaining sample volume (of the initial 150 mL) for the last data point in the MOX 24% Experiment 2 is 47 mL, the specific production rate is $3.16 \cdot 10^{-6}$ mol/L·d. This gives a yield between dissolution and radiolytic production of 61%. However, as the dissolution rate is considerably lower during the early stages of the experiment, the overall yield is much lower, at approximately 15%.

The dissolution rate for the low-doped MOX 10% Experiment 2 is $5.91 \cdot 10^{-7}$ M·d$^{-1}$ after an initial time period of 50 days, which is approximately a factor of 3.6 lower as compared to the MOX 24% experiments. This corresponds very well to the ratio in radiolytic production between the 24% and average production of the 10% pellets of ($1.49 \cdot 10^{-7}$ mol/d/)/($4.29 \cdot 10^{-8}$ mol/d)=3.5. The specific radiolytic production rate for the last data point in the MOX 10% Experiment 2 is $9.45 \cdot 10^{-7}$ mol/L·d (in 45 mL solution), which corresponds to a yield between dissolution and radiolytic production of 63%. The initial solution volume in the MOX 10% Experiment 1 was 250 mL, varying from the

volumes in the other Ar atmosphere experiments of 150 mL. This affects the dissolution rate at the end of the experiment, which is equal to $2.10 \cdot 10^{-7}$ M·d$^{-1}$, significantly lower than that of the MOX 10% Experiment 2. The specific production of $H_2O_2$ for the final point in the MOX 10% Experiment 1 is however $2.44 \cdot 10^{-7}$ mol/L·d (176 mL), giving a yield between dissolution and radiolytic production of 86%. The $H_2O_2$ concentration in solution was measured at the end of the autoclave experiments and gave concentrations below the detection limit of the Ghormley method (~$2 \cdot 10^{-6}$ M).

The initial phase with slow non-linear oxidative dissolution in the MOX 10% Experiment 2 is followed by a phase of linear oxidative dissolution with a coefficient of determination, $r^2$=0.992, as can be seen in Figure 25. As sampling is performed, the volume in the autoclave decreases and the specific production of $H_2O_2$ in solution should increase as the radiolytic production rate is constant. This should result in a faster oxidation and dissolution rate, which was not observed during the experiment. A linear dissolution trend was also observed in the other Ar atmosphere experiments, however with somewhat worse linear fits.

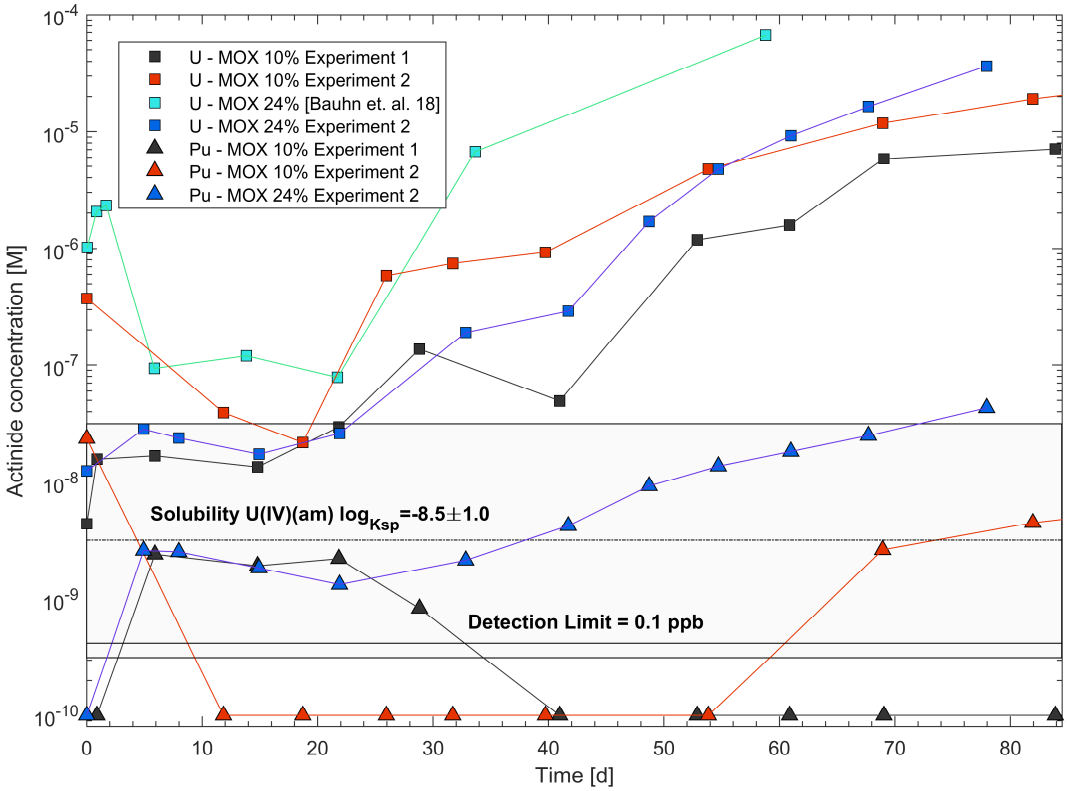


*Figure 24 - 10 and 24 wt% Pu-doped leaching experiments under 10 bar initial argon atmospheres shown together with the data from Bauhn et. al. [70]. The full MOX 10% Experiment 2 series is not shown.*

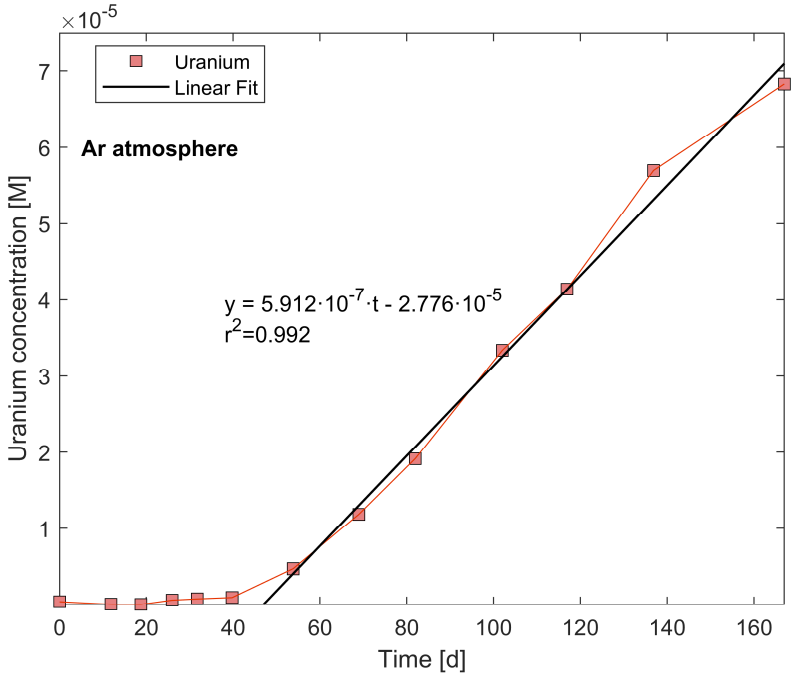


*Figure 25 - Entire 10 bar Ar MOX 10% Experiment 2 series with the corresponding linear fit after the initial 54 days.*

In a study by Odorowski et. al., the oxidative dissolution of 7 wt% Pu-doped MOX was investigated under Ar and air atmospheres. The Ar atmosphere showed no significant difference as compared to exposing the solution to air atmosphere. This is indicative of the radiolytic oxidation playing a much larger part in the oxidation process than the oxidation from air. The dissolution rates followed a linear trend from the start of the experiment and there was no lag period as seen in this work. This could be due to a difference in sample preparation, as the researchers used carbonate washing steps after the annealing. The delay seen in this work could possibly be explained by the presence of a nitride phase. Redox potential was measured by Odorowski et. al. ex-situ with an electrode. The measurement showed a higher redox potential for the Ar-atmosphere experiment, which is unexpected, but the difference is likely within the uncertainty of the measurement [71].

### 6.4.4. 10 wt% Pu-doped MOX experiment under 8 bar D2 atmosphere

A 10 wt% Pu-doped MOX pellet was studied in 10 mM NaCl + 2 mM $NaHCO_3$ solution under 8 bar $D_2$ atmosphere. $D_2$ was used instead of $H_2$ in order to be able to isotopically label the reactions that the dissolved hydrogen takes part in. The dissolution rate of the 10 wt% Pu-doped MOX pellet was considerably lower under $D_2$ atmosphere as compared to under Ar atmosphere (Figure 26). The uranium concentration stops increasing significantly after 74 days, at a concentration of approximately $4 \cdot 10^{-7}$ M. The concentration drops to approximately $3 \cdot 10^{-7}$ M after 136 days. The concentrations of Pu are below the detection limit in the analysed samples for almost the entirety of the experiment, due to heavy sorption to the walls of the glass beaker and on the stainless-steel

dip tube. The $H_2O_2$ concentration in solution was measured at the end of the autoclave experiment and gave a concentration below the detection limit of the Ghormley method (~$2 \cdot 10^{-6}$ M).

Visible amounts of amber colored Fe-precipitate were found at the end of the experiment upon opening the autoclave. However, during the sampling procedure this precipitation was not noticeable through visual inspection, likely due to the precipitation being located at the bottom of the beaker and not efficiently mixing into the sampling solution. The precipitate likely comes from corrosion of the dip tube or other stainless-steel components. The occurrence of the precipitate would likely explain the decrease in dissolved uranium concentration in solution, as Fe(II)-containing solid phases can reduce U(VI). However, the precipitate has the visual appearance of a Fe(III)-containing mineral, such as haematite or goethite [91], which might have been produced through the oxidation of Fe(II). The result is relevant for the final repository conditions as massive iron inserts are included in the copper canister, providing a source of Fe(II). No indication of Fe-precipitation was observed under the Ar atmosphere experiments, suggesting that the $D_2$ atmosphere influenced the corrosion of the stainless-steel components of the autoclave system.

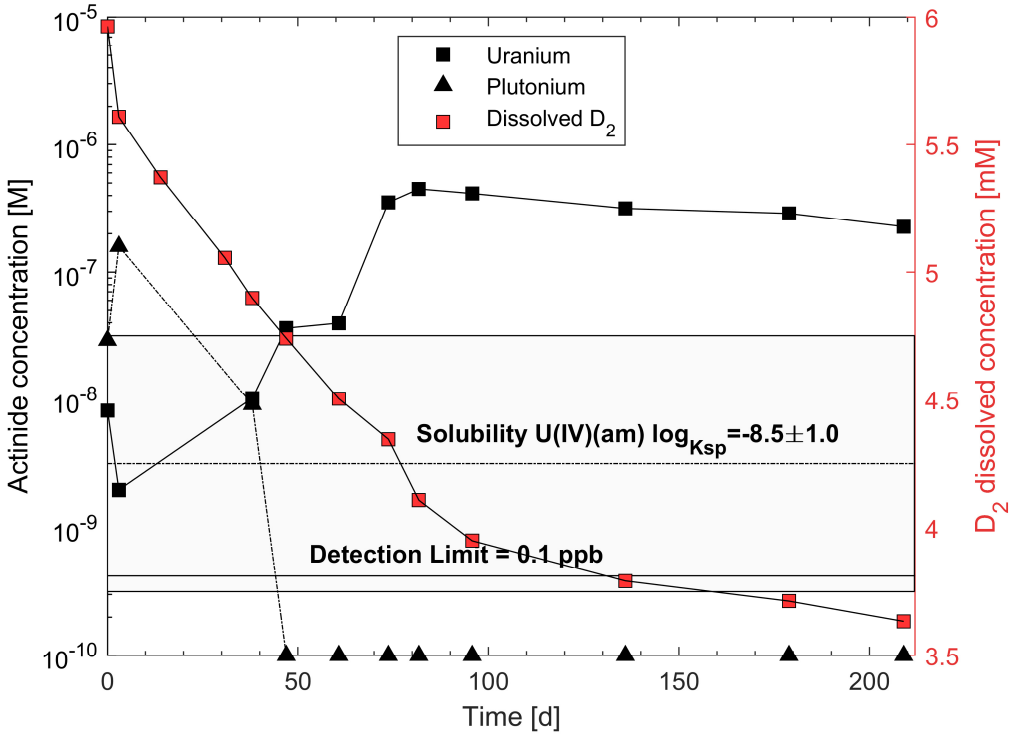


*Figure 26 - 10 wt% Pu-doped MOX under 8 bar initial $D_2$ pressure. The solution consists of 10 mM NaCl and 2mM $NaHCO_3$.*

### 6.4.5. 24 wt% Pu-doped MOX experiment under 15 bar D2 atmosphere

The 15 bar $D_2$ MOX experiment was performed with the 24 wt% Pu-doped MOX pellet in 10 mM NaCl + 2 mM $NaHCO_3$ solution. The initial dissolution rate was very high, as can be seen in Figure 27, likely indicative of air leaking in. The autoclave pressure also reflected some degree of leakage, as the pressure dropped from 11.5 bar to 11.0 bar $D_2$ between the fourth and fifth sampling.

However, the uranium concentration dropped dramatically in the last data point at the end of the experiment, below the detection limit of the ICP-MS measurement, as indicated in Figure 27. Significant amounts of Fe-precipitation were found at the end of the experiment upon opening of the autoclave. The dissolved uranium concentration is clearly affected by the corrosion of the stainless-steel components of the autoclave system. The $H_2O_2$ concentration in solution was measured at the end of the autoclave experiments and gave concentrations below the detection limit of the Ghormley method (~$2 \cdot 10^{-6}$ M).

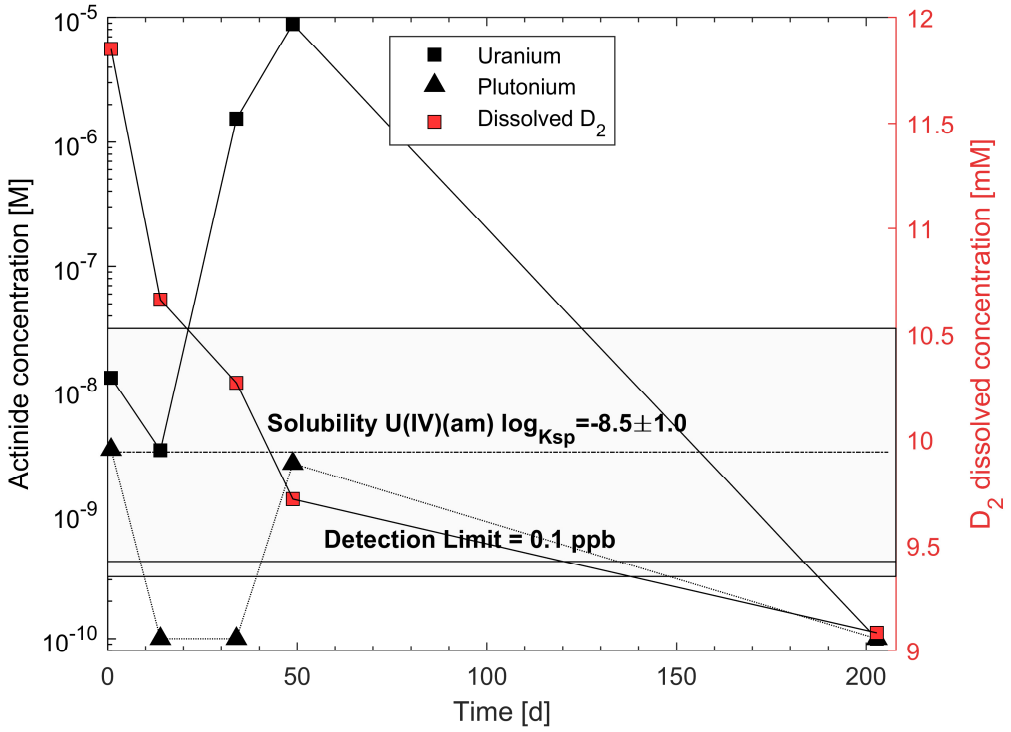


*Figure 27 - 15 bar $D_2$ experiment using the 24 wt% Pu-doped MOX pellet. The dissolved uranium concentration is affected by the corrosion of the stainless-steel components of the autoclave system.*

## 6.5. SIMFUEL oxidation studies under $D_2$ atmosphere

In the SIMFUEL experiment, $H_2O_2$ was spiked into the 100 mL solution, resulting in a concentration of 2.5 mM at the start of the experiment. The autoclave was pressurized to 10 bar $D_2$. The matrix was resistant to oxidative dissolution, as shown by the low dissolved uranium to consumed $H_2O_2$ as shown in Figure 28. The average uranium dissolution to $H_2O_2$ consumption under these conditions is $1.69 \cdot 10^{-6}$ %, showing that $UO_2$ doped with ε-particles under hydrogen atmosphere is highly efficient at decomposing $H_2O_2$ without causing oxidation of the $UO_2$ matrix. This is highly relevant to the final repository water intrusion scenario and shows that the metallic ε-particle inclusions are important for the stability of spent fuel under oxidizing conditions. However, the yield between dissolution and $H_2O_2$ consumption are strongly dependent on the amount of $H_2O_2$ spiked into solution as seen in the work of de Pablo et. al. [85]. Under high concentrations $H_2O_2$, the dissolution rate plateaus, and an increase of $H_2O_2$ only leads to a higher

amount of decomposition. The low ratio between uranium dissolved divided by $H_2O_2$ consumed is therefore also due to a high amount of decomposition due to the high initial concentration.

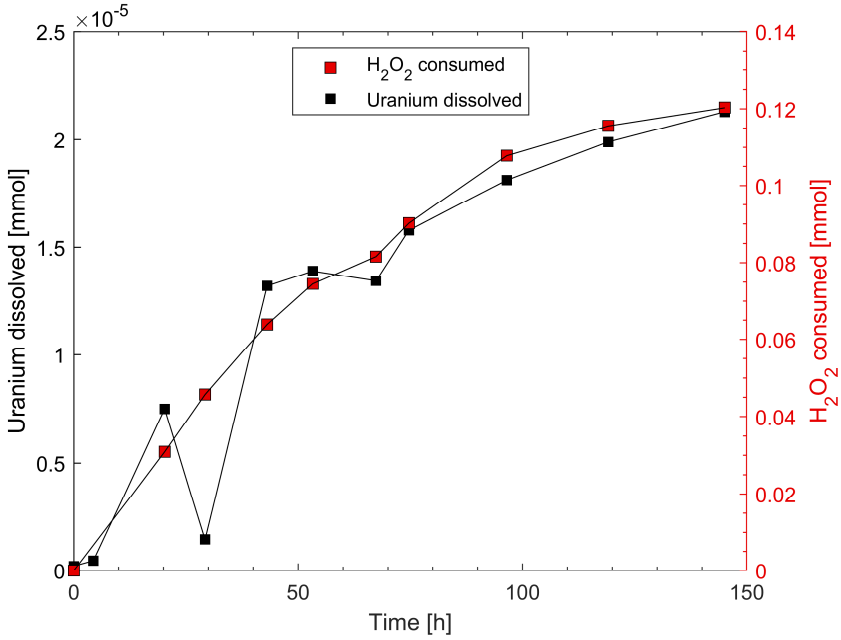


*Figure 28 - Dissolved uranium from the SIMFUEL pellet under $D_2$ atmosphere using additions of $H_2O_2$. The consumed $H_2O_2$ is also shown as a function of time.*

## 6.6. Fe-Ca-UO2-CO3-system

A uranyl stock solution was mixed with 10 mM NaCl + 2 mM $NaHCO_3$ and 9 mM NaCl + 1.5 mM $NaHCO_3$ + 0.5 mM $CaCO_3$ solutions in two separate vials, resulting in initial uranium concentrations of $4.5 \cdot 10^{-6}$ M at the start of the experiments. Using the solubility product of $CaCO_3$ stated in the work of Coto et. al. of $(5.25 \pm 0.65) \cdot 10^{-4}$ M at 25°C [55], both systems were calculated to have an ionic strength of ~0.012 ($mol \cdot kg^{-1}$). This was done to minimize the effect of activity coefficients, which would have influenced the apparent stability constants of the complex formation reactions in solution [92]. Both the carbonate systems are shown in Figure 29. In contact with the polished ~0.14g iron foil pieces with 3.64 $cm^2$ surface area, the dissolved uranium concentrations decreased quite rapidly during the initial stages of the experiment in both solutions. In the carbonate uranyl experiment containing calcium, the concentration apparently stabilized around $2\text{-}3 \cdot 10^{-8}$ M, while in the carbonate uranyl experiment, the uranium concentration dropped below the detection limit. As these results are only from one experimental series conducted in a glove box with ≤1 ppm $O_2$, the results should be regarded as preliminary.

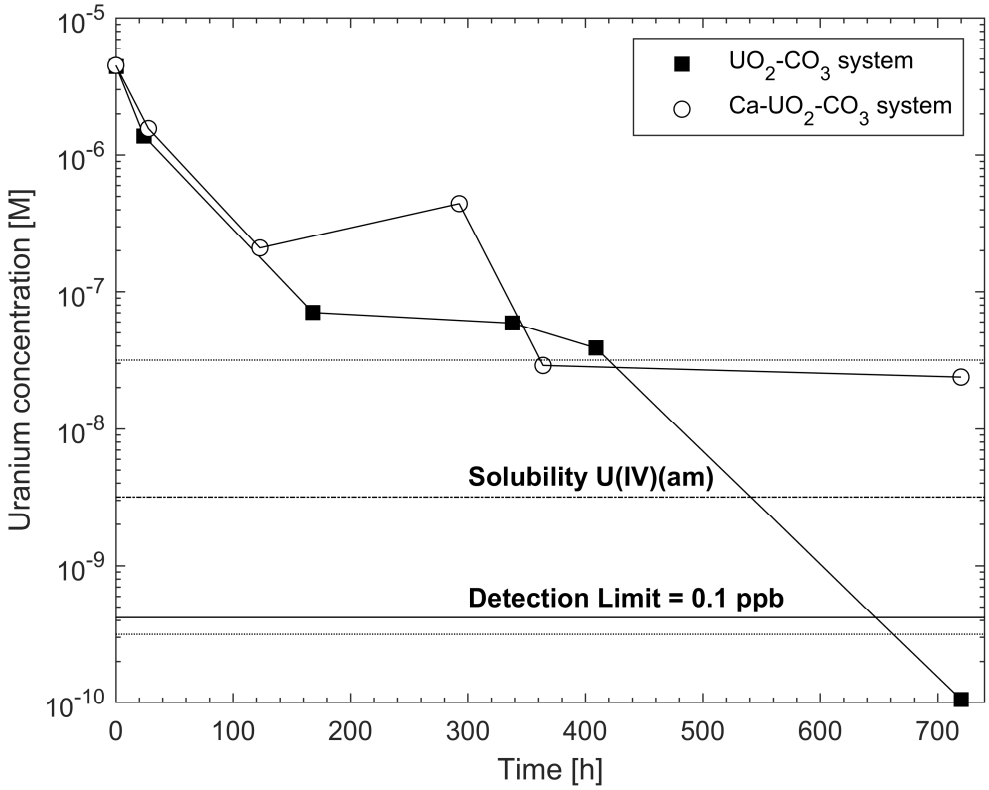


*Figure 29 – The uranium concentration of the 10 mM NaCl + 2 mM $NaHCO_3$ (■) and 9 mM NaCl + 1.5 mM $NaHCO_3$ + 0.5 mM $CaCO_3$ solution (○) experiments in contact with a piece of iron foil as a function of time. The last data point in the $UO_2$-$CO_3$ system corresponds to a concentration below the detection limit.*

# 7. Conclusions

The safety of the KBS-3 repository concept is highly dependent on the redox conditions at the fuel surface-liquid interface under the water intrusion scenario. Exposing a 30 µm thick water layer next to the $UO_2$ pellet surfaces to a 1.85 MBq Am-241 source under both Ar and $H_2$ atmospheres resulted in no noticeable oxidation of the pellet surfaces. This indicates that the source is too weak to cause sufficient oxidation to overcome the dissolution rate in MQ water. The 3.30 MBq Am-241 source, however, was sufficiently strong to significantly oxidize the $UO_2$ surfaces under Ar atmosphere. The $H_2$ atmosphere had a suppressing effect on the surface oxidation of the $UO_2$ pellets that were exposed to the 3.30 MBq external Am-241 source. In the measurement of a surface oxidation state before and after exposure to the 3.30 MBq source for 11 days under $H_2$ atmosphere, no increase in surface oxidation was noted. The oxidative dissolution was also suppressed by the $H_2$ atmosphere by roughly a factor of 10 as compared to the uranium dissolution under Ar atmosphere.

The oxidative dissolution studies of MOX pellets showed a significantly different dissolution rate under $D_2$ atmosphere as compared to Ar atmosphere. However, under $D_2$ atmosphere the stainless-steel components of the autoclave showed signs of corrosion, which likely caused the drops in uranium and plutonium concentrations in the 10 mM NaCl and 2 mM $NaHCO_3$ solution. This shows the efficient reduction of dissolved uranium in the presence of corroding iron. The ratio between uranium dissolution and $H_2O_2$ consumption was approximately ~70% under Ar atmosphere by the end of the experiments. This was determined using the ASTAR mass stopping power data with the geometrical calculation model developed in this work to calculate the production of $H_2O_2$. The SIMFUEL pellet exposed to a high concentration of $H_2O_2$ under $D_2$ atmosphere yielded a very low ratio of dissolved uranium to consumed $H_2O_2$, showing that the metallic ε-particle inclusions on the $UO_2$ pellet significantly activate the protective effect of $H_2$. This shows that even under high concentrations of $H_2O_2$, spent fuel will likely undergo oxidative dissolution to a low extent under a water intrusion scenario.

A preliminary experiment indicates that the presence of Ca influences the reduction or precipitation of the $UO_2(CO_3)_2^{2-}$ and $UO_2(CO_3)_3^{4-}$ complexes in the presence of an Fe(II)-containing foil through the formation of $CaUO_2(CO_3)_3^{2-}$ and $Ca_2UO_2(CO_3)_3$.

## Future work

The results of the XPS study should be further investigated by performing another exposure experiment of a $UO_2$ pellet to the 3.30 MBq Am-241 source under $H_2$ atmosphere.

The MOX autoclave experiments under $H_2$ atmosphere will be repeated, either using a new autoclave without corroded stainless-steel surfaces or components, or using plastic components in contact with solution, so that the effect of $H_2$ can be studied. MOX experiments will also be performed in the presence of iron foils, as well as magnetite, to study the reducing effect of iron, which is highly relevant for the water intrusion scenario.

Further investigations will be performed on the effect of Ca on the $UO_2$-$CO_3$ complex speciation in the presence of Fe(II)-containing surfaces. The partial pressure of $O_2$ will be controlled to a much larger extent to minimize any influence of a continuous supply of $O_2$.

# Acknowledgements

The Swedish Nuclear Fuel and Waste Management Company, SKB, is gratefully acknowledged for funding this project.

Thanks to Kastriot, Christian and Eric for valuable discussions and support in my work. I'd also like to thank Lovisa for valuable discussions and for introducing me to the topic and letting me be part of her interesting research.

Thanks to all my colleagues who makes the fikas, lunches, after works and the time at Chalmers wonderful. A big thanks to my office mates Marcus and Thea for great feedback and discussions about the work and many other topics.

I'd also like to thank my mom, dad, brother and cat for all their love and support.

Last but not least, a very special thanks to my future wife Olivia for all her love, support and sense of humor.

# References


1. Marcus, G.H., *Nuclear power around the world.* Nature Reviews Physics, 2019. **1**(3): p. 172.
2. World Nuclear Association, *World Nuclear Performance Report*. 2019.
3. IAEA, *Nuclear Share of Electricity Generation*, in *Power Reactor Information System*. 2019.
4. Aaltonen, I., et al., *Geology of Olkiluoto.* Posiva Report, 2016. **2016-16**.
5. Svensk Kärnbränslehantering AB, *Technical Report TR 11-01 - Long-term safety for the final repository for spent nuclear fuel at Forsmark.* 2011.
6. Holden, N., *Isotopic composition of the elements and their variation in nature: a preliminary report*. 1977, Brookhaven National Lab.
7. Bera, S., et al., *Oxidation state of uranium: an XPS study of alkali and alkaline earth uranates.* Journal of Nuclear Materials, 1998. **255**(1): p. 26-33.
8. Ekstrom, A., *Kinetics and mechanism of the disproportionation of uranium (V).* Inorganic Chemistry, 1974. **13**(9): p. 2237-2241.
9. Morss, L.R., et al., *The chemistry of the actinide and transactinide elements*. Vol. 1. 2006: Springer.
10. Grenthe, I., et al., *Uranium*, in *The chemistry of the actinide and transactinide elements*. 2008, Springer. p. 253-698.
11. Boczar, P. and M. Van Dyk, *Improved locations of reactivity devices in future CANDU reactors fuelled with natural uranium or enriched fuels*. 1987, Atomic Energy of Canada Ltd.
12. Shoesmith, D., *Fuel corrosion processes under waste disposal conditions.* Journal of Nuclear Materials, 2000. **282**(1): p. 1-31.
13. Choppin, G., et al., *Chapter 19 - Principles of Nuclear Power*, in *Radiochemistry and Nuclear Chemistry (Fourth Edition)*. 2013, Academic Press: Oxford. p. 595-653.
14. Teterin, Y.A., et al., *XPS study of ion irradiated and unirradiated UO2 thin films.* Inorganic chemistry, 2016. **55**(16): p. 8059-8070.
15. Wagemans, C., *The nuclear fission process*. 1991: CRC press.
16. Diven, B., et al., *Multiplicities of fission neutrons.* Physical Review, 1956. **101**(3): p. 1012.
17. Choppin, G., et al., *Chapter 17 - Production of Radionuclides*, in *Radiochemistry and Nuclear Chemistry (Fourth Edition)*. 2013, Academic Press: Oxford. p. 513-544.
18. Holm, M., *RadTox, a computer program for assessing radiotoxicity curves for used nuclear fuel.* Chalmers University of Technology, Department of Nuclear Chemistry, Master's thesis, 2011.
19. Kleykamp, H., *The solubility of selected fission products in UO 2 and (U, Pu) O 2.* Journal of Nuclear Materials, 1993. **206**(1): p. 82-86.

20. Johnson, L., et al., *Spent fuel radionuclide source-term model for assessing spent fuel performance in geological disposal. Part I: Assessment of the instant release fraction.* Journal of Nuclear Materials, 2005. **346**(1): p. 56-65.

21. Näslund, J.-O., J. Brandefelt, and L.C. Liljedahl, *Climate considerations in long-term safety assessments for nuclear waste repositories.* Ambio, 2013. **42**(4): p. 393-401.

22. Brookins, D., *Radionuclide behavior at the Oklo nuclear reactor, Gabon.* Waste Management, 1990. **10**(4): p. 285-296.

23. Menet, C., M.-T. Ménager, and J.-C. Petit, *Migration of radioelements around the new nuclear reactors at Oklo: analogies with a high-level waste repository.* Radiochimica Acta, 1992. **58**(2): p. 395-400.

24. Kolář, M. and F. King. *Modelling the consumption of oxygen by container corrosion and reaction with Fe (II)*. in *MRS Proceedings*. 1995. Cambridge Univ Press.

25. Neck, V. and J. Kim, *Solubility and hydrolysis of tetravalent actinides.* Radiochimica Acta, 2001. **89**(1): p. 1-16.

26. Choppin, G., et al., *Chapter 8 - Radiation Effects on Matter*, in *Radiochemistry and Nuclear Chemistry (Fourth Edition)*. 2013, Academic Press: Oxford. p. 209-237.

27. Christensen, H., *Calculations simulating spent-fuel leaching experiments.* Nuclear technology, 1998. **124**(2): p. 165-174.

28. Werme, L.O., et al., *Spent fuel performance under repository conditions: A model for use in SR-Can*. 2004, Swedish Nuclear Fuel and Waste Management Co.

29. Ekeroth, E., O. Roth, and M. Jonsson, *The relative impact of radiolysis products in radiation induced oxidative dissolution of UO2.* Journal of Nuclear Materials, 2006. **355**(1-3): p. 38-46.

30. Bauhn, L., et al., *The fate of hydroxyl radicals produced during H2O2 decomposition on a SIMFUEL surface in the presence of dissolved hydrogen.* Journal of Nuclear Materials, 2018. **507**: p. 38-43.

31. Nilsson, S. and M. Jonsson, *H2O2 and radiation induced dissolution of UO2 and SIMFUEL pellets.* Journal of Nuclear Materials, 2011. **410**(1-3): p. 89-93.

32. Ziegler, J., *Stopping of energetic light ions in elemental matter.* Journal of applied physics, 1999. **85**(3): p. 1249-1272.

33. Bethe, H., *Zur theorie des durchgangs schneller korpuskularstrahlen durch materie.* Annalen der Physik, 1930. **397**(3): p. 325-400.

34. Lindhard, J., M. Scharff, and H.E. Schiøtt, *Range concepts and heavy ion ranges*. 1963: Munksgaard Copenhagen.

35. Toftegaard, J., et al. *Improvements in the stopping power library libdEdx and release of the web GUI dedx. au. dk*. in *Journal of Physics: Conference Series*. 2014. IOP Publishing.

36. Hansson, N.L., C. Ekberg, and K. Spahiu, *Alpha Dose Rate Calculations for UO2 Based Materials using Stopping Power Models.* Nuclear Materials and Energy, Accepted, 2020.

37. Neretnieks, I., *Some aspects of the use of iron canisters in deep lying repositories for nuclear waste*. 1985: Nagra.

38. Bonin, B., M. Colin, and A. Dutfoy, *Pressure building during the early stages of gas production in a radioactive waste repository.* Journal of Nuclear Materials, 2000. **281**(1): p. 1-14.

39. Amme, M., et al., *Combined effects of Fe (II) and oxidizing radiolysis products on UO2 and PuO2 dissolution in a system containing solid UO2 and PuO2.* Journal of Nuclear Materials, 2012. **430**(1-3): p. 1-5.

40. Cui, D. and K. Spahiu, *The reduction of U (VI) on corroded iron under anoxic conditions.* Radiochimica Acta, 2002. **90**(9-11): p. 623-628.

41. Odorowski, M., et al., *Effect of metallic iron on the oxidative dissolution of UO2 doped with a radioactive alpha emitter in synthetic Callovian-Oxfordian groundwater.* Geochimica et Cosmochimica Acta, 2017. **219**: p. 1-21.

42. Carbol, P., et al., *Hydrogen suppresses UO2 corrosion.* Geochimica et Cosmochimica Acta, 2009. **73**(15): p. 4366-4375.

43. Spahiu, K., et al., *The reduction of U(VI) by near field hydrogen in the presence of UO2 (s).* Radiochimica Acta, 2004. **92**(9-11): p. 597-601.

44. Saillard, J.Y. and R. Hoffmann, *Carbon-hydrogen and hydrogen-hydrogen activation in transition metal complexes and on surfaces.* Journal of the American Chemical Society, 1984. **106**(7): p. 2006-2026.

45. Bauhn, L., et al., *The Effect of Bromide on Oxygen Yields in Homogeneous α-radiolysis.* MRS Advances, 2017. **2**(13): p. 711-716.

46. Brown, P.L. and C. Ekberg, *Hydrolysis of metal ions*. 2016: John Wiley & Sons.

47. Sunder, S., N. Miller, and D. Shoesmith, *Corrosion of uranium dioxide in hydrogen peroxide solutions.* Corrosion Science, 2004. **46**(5): p. 1095-1111.

48. Einziger, R., et al., *Oxidation of spent fuel in air at 175 to 195 C.* Journal of nuclear materials, 1992. **190**: p. 53-60.

49. Santos, B., et al., *X-ray photoelectron spectroscopy study of anodically oxidized SIMFUEL surfaces.* Electrochimica acta, 2004. **49**(11): p. 1863-1873.

50. Sunder, S., G. Boyer, and N. Miller, *XPS studies of UO2 oxidation by alpha radiolysis of water at 100 C.* Journal of Nuclear Materials, 1990. **175**(3): p. 163-169.

51. Leinders, G., et al., *Evolution of the uranium chemical state in mixed-valence oxides.* Inorganic chemistry, 2017. **56**(12): p. 6784-6787.

52. Kvashnina, K., et al., *Chemical state of complex uranium oxides.* Physical review letters, 2013. **111**(25): p. 253002.

53. Song, K.W., et al., *Sintering of mixed UO2 and U3O8 powder compacts.* Journal of nuclear materials, 2000. **277**(2-3): p. 123-129.

54. Smellie, J., M. Laaksoharju, and P. Wikberg, *Äspö, SE Sweden: a natural groundwater flow model derived from hydrogeochemical observations.* Journal of Hydrology, 1995. **172**(1-4): p. 147-169.

55. Coto, B., et al., *Effects in the solubility of CaCO3: Experimental study and model description.* Fluid Phase Equilibria, 2012. **324**: p. 1-7.

56. Shoesmith, D., et al., *The corrosion of nuclear fuel (UO2) in oxygenated solutions.* Corrosion Science, 1989. **29**(9): p. 1115-1128.

57. Lower SK, *Carbonate equilibria in natural waters– A Chem1 Reference Text, Simon Fraser University, 1999.*

58. Schenk, H., et al., *Development of sorbers for the recovery of uranium from seawater. 1. Assessment of key parameters and screening studies of sorber materials.* Separation Science and Technology, 1982. **17**(11): p. 1293-1308.

59. Endrizzi, F. and L. Rao, *Chemical speciation of uranium (VI) in marine environments: complexation of calcium and magnesium Ions with [(UO2)(CO3) 3] 4− and the effect on the extraction of uranium from seawater.* Chemistry–A European Journal, 2014. **20**(44): p. 14499-14506.

60. Bernhard, G., et al., *Speciation of uranium in seepage waters of a mine tailing pile studied by time-resolved laser-induced fluorescence spectroscopy (TRLFS).* Radiochimica Acta, 1996. **74**(s1): p. 87-92.

61. Kalmykov, S.N. and G.R. Choppin, *Mixed Ca2+/UO22+/CO32-complex formation at different ionic strengths.* Radiochimica Acta, 2000. **88**(9-11): p. 603-608.

62. Bernhard, G., et al., *Uranyl (VI) carbonate complex formation: Validation of the Ca2UO2 (CO3) 3 (aq.) species.* Radiochimica Acta, 2001. **89**(8): p. 511-518.

63. Dong, W. and S.C. Brooks, *Determination of the formation constants of ternary complexes of uranyl and carbonate with alkaline earth metals (Mg2+, Ca2+, Sr2+, and Ba2+) using anion exchange method.* Environmental science & technology, 2006. **40**(15): p. 4689-4695.

64. Stewart, B.D., M.A. Mayes, and S. Fendorf, *Impact of uranyl− calcium− carbonato complexes on uranium (VI) adsorption to synthetic and natural sediments.* Environmental science & technology, 2010. **44**(3): p. 928-934.

65. Barr, T.L., *Modern ESCAThe Principles and Practice of X-Ray Photoelectron Spectroscopy*. 1994: CRC press.

66. Hollander, J.M. and W.L. Jolly, *X-ray photoelectron spectroscopy.* Accounts of chemical research, 1970. **3**(6): p. 193-200.

67. Ilton, E.S. and P.S. Bagus, *XPS determination of uranium oxidation states.* Surface and Interface Analysis, 2011. **43**(13): p. 1549-1560.

68. Cox, L. and J. Farr, *4f binding-energy shifts of the light-actinide dioxides and tetrafluorides.* Physical Review B, 1989. **39**(15): p. 11142.

69. Ilton, E.S., et al., *Mica surfaces stabilize pentavalent uranium.* Inorganic chemistry, 2005. **44**(9): p. 2986-2988.

70. Bauhn, L., et al., *The interaction of molecular hydrogen with α-radiolytic oxidants on a (U,Pu)O2 surface.* Journal of Nuclear Materials, 2018. **505**: p. 54-61.

71. Odorowski, M., et al., *Oxidative dissolution of unirradiated Mimas MOX fuel (U/Pu oxides) in carbonated water under oxic and anoxic conditions.* Journal of Nuclear Materials, 2016. **468**: p. 17-25.

72. Lucuta, P., et al., *Microstructural features of SIMFUEL—simulated high-burnup UO2-based nuclear fuel.* Journal of Nuclear Materials, 1991. **178**(1): p. 48-60.

73. Willey, T.M., et al., *Rapid degradation of alkanethiol-based self-assembled monolayers on gold in ambient laboratory conditions.* Surface Science, 2005. **576**(1): p. 188-196.

74. Allen, A.O., et al., *Decomposition of water and aqueous solutions under mixed fast neutron and γ-radiation.* The Journal of Physical Chemistry, 1952. **56**(5): p. 575-586.

75. Hochanadel, C., *Effects of cobalt γ-radiation on water and aqueous solutions.* The Journal of Physical Chemistry, 1952. **56**(5): p. 587-594.

76. Ghormley, J. and A. Stewart, *Effects of γ-Radiation on Ice1.* Journal of the American Chemical Society, 1956. **78**(13): p. 2934-2939.

77. International Commission on Radiation Units, *ICRU Report*. 1956: International Commission on Radioation Units and Measurements.

78. Emfietzoglou, D., et al., *Subcellular S-factors for low-energy electrons: a comparison of Monte Carlo simulations and continuous-slowing-down calculations.* 2008. **84**(12): p. 1034-1044.

79. Seah, M., *Summary of ISO/TC 201 Standard: VII ISO 15472: 2001—surface chemical analysis—x-ray photoelectron spectrometers—calibration of energy scales.* Surface and Interface Analysis: An International Journal devoted to the development and application of techniques for the analysis of surfaces, interfaces and thin films, 2001. **31**(8): p. 721-723.

80. Grivet, J.-P., *Accurate numerical approximation to the Gauss–Lorentz lineshape.* Journal of Magnetic Resonance, 1997. **125**(1): p. 102-106.

81. Shirley, D.A., *High-resolution X-ray photoemission spectrum of the valence bands of gold.* Physical Review B, 1972. **5**(12): p. 4709.

82. Maslakov, K.I., et al., *XPS study of uranium-containing sodium-aluminum-iron-phosphate glasses.* Journal of Alloys and Compounds, 2017. **712**: p. 36-43.

83. Van den Berghe, S., et al., *XPS investigations on cesium uranates: mixed valency behaviour of uranium.* Journal of nuclear materials, 2000. **277**(1): p. 28-36.

84. Grenthe, I., et al., *Studies on metal carbonate equilibria. Part 10. A solubility study of the complex formation in the uranium (VI)–water–carbon dioxide (g) system at 25° C.* Journal of the Chemical Society, Dalton Transactions, 1984(11): p. 2439-2443.

85. De Pablo, J., et al., *The effect of hydrogen peroxide concentration on the oxidative dissolution of unirradiated uranium dioxide.* MRS Online Proceedings Library Archive, 2000. **663**.

86. De Pablo, J., et al., *Solid surface evolution model to predict uranium release from unirradiated UO2 and nuclear spent fuel dissolution under oxidizing conditions.* Journal of nuclear materials, 1996. **232**(2-3): p. 138-145.

87. Sunder, S., G.D. Boyer, and N.H. Miller, *XPS Studies of UO2 oxidation by alpha radiolysis of water at 100°C.* Journal of Nuclear Materials, 1990. **175**(3): p. 163-169.

88. Delobel, R., et al., *X-ray photoelectron spectroscopy study of uranium and antimony mixed metal-oxide catalysts.* Journal of the Chemical Society, Faraday Transactions 1: Physical Chemistry in Condensed Phases, 1983. **79**(4): p. 879-891.

89. McIntyre, N., et al., *Chemical information from XPS—applications to the analysis of electrode surfaces.* Journal of Vacuum Science and Technology, 1981. **18**(3): p. 714-721.

90. Fors, P., *The effect of dissolved hydrogen on spent nuclear fuel corrosion*. 2009: Chalmers University of Technology.

91. Schwertmann, U., *Transformation of hematite to goethite in soils.* Nature, 1971. **232**(5313): p. 624-625.

92. Grenthe, I. and H. Wanner, *Guidelines for the extrapolation to zero ionic strength.* 2000.